The XXL Survey. XLII. The $L_X - \sigma_v$ relation of galaxy groups and clusters detected in the *XXL* and *GAMA* surveys

P. A. Giles [1,2]★ A. Robotham [3] M. E. Ramos-Ceja [4,5] B. J. Maughan [2] M. Sereno [6,7]
S. McGee [8] S. Phillipps [2] A. Iovino [9] D. J. Turner [1] C. Adami,[10] S. Brough [11] L. Chiappetti [12]
S. P. Driver [13] A. E. Evrard [14] A. Farahi [15,16] F. Gastaldello [12] B. W. Holwerda [17]
A. M. Hopkins [18] E. Koulouridis [19] F. Pacaud,[4] M. Pierre[20] and K. A. Pimbblet[21]

[1]*Department of Physics and Astronomy, University of Sussex, Brighton BN1 9QH, UK*
[2]*School of Physics, HH Wills Physics Laboratory, Tyndall Avenue, Bristol BS8 1TL, UK*
[3]*ICRAR, M468, University of Western Australia, Crawley WA 6009, Australia*
[4]*Argelander-Institut fur Astronomie, University of Bonn, Auf dem Hugel 71, D-53121 Bonn, Germany*
[5]*Max-Planck Institut für extraterrestrische Physik, Postfach 1312, D-85741 Garching bei München, Germany*
[6]*INAF – Osservatorio di Astrofisica e Scienza dello Spazio di Bologna, via Piero Gobetti 93/3, I-40129 Bologna, Italy*
[7]*INFN, Sezione di Bologna, viale Berti Pichat 6/2, I-40127 Bologna, Italy*
[8]*School of Physics and Astronomy, University of Birmingham, Edgbaston, Birmingham B15 2TT, UK*
[9]*INAF, Osservatorio Astronomico di Brera, Via Brera 28, I-20122 Milano, Italy*
[10]*Université Aix-Marseille, CNRS, LAM (Laboratoire d'Astrophysique de Marseille) UMR 7326, F-13388 Marseille, France*
[11]*School of Physics, University of New South Wales, NSW 2052, Australia*
[12]*INAF - IASF Milan, via A. Corti 12, I-20133 Milano, Italy*
[13]*University of Western Australia, 35 Stirling Highway, Carley, Perth WA 6009, Australia*
[14]*Physics and Leinweber Center for Theoretical Physics, University of Michigan, Ann Arbor, MI 48109, USA*
[15]*The Michigan Institute for Data Science, University of Michigan, Ann Arbor, MI 48109, USA*
[16]*Department of Astronomy, University of Michigan, Ann Arbor, MI 48109, USA*
[17]*Department of Physics and Astronomy, 102 Natural Science Building, University of Louisville, Louisville KY 40292, USA*
[18]*Australian Astronomical Optics, Macquarie University, 105 Delhi Rd, North Ryde, NSW 2113, Australia*
[19]*Institute for Astronomy & Astrophysics, Space Applications & Remote Sensing, National Observatory of Athens, GR-15236 Palaia Penteli, Greece*
[20]*AIM, CEA, CNRS, Université Paris-Saclay, Université Paris Diderot, Sorbonne Paris Cité, F-91191 Gif-sur-Yvette, France*
[21]*E.A. Milne Centre for Astrophysics, University of Hull, Cottingham Road, Kingston-upon-Hull HU6 7RX, UK*

ABSTRACT

The *XXL* Survey is the largest homogeneous survey carried out with *XMM-Newton*. Covering an area of 50 deg^2, the survey contains several hundred galaxy clusters out to a redshift of ≈ 2, above an X-ray flux limit of $\sim 6 \times 10^{-15}$ er g cm^{-2} s^{-1}. The GAMA spectroscopic survey of $\sim 300\,000$ galaxies covers ≈ 286 deg^2, down to an r-band magnitude of $r < 19.8$ mag. The region of overlap of these two surveys (covering 14.6 deg^2) represents an ideal opportunity to study clusters selected via two independent selection criteria. Generating two independently selected samples of clusters, one drawn from XXL (spanning a redshift range $0.05 \leq z \leq 0.3$) and another from GAMA ($0.05 \leq z \leq 0.2$), both spanning $0.2 \lesssim M_{500} \lesssim 5 \times 10^{14}\,\mathrm{M_\odot}$, we investigate the relationship between X-ray luminosity and velocity dispersion ($L_X - \sigma_v$ relation). Comparing the $L_X - \sigma_v$ relation between the X-ray selected and optically selected samples, when not accounting for the X-ray selection, we find that the scatter of the X-ray selected sample is 2.7 times higher than the optically selected sample (at the 3.7σ level). Accounting for the X-ray selection to model the $L_X - \sigma_v$ relation, we find that the difference in the scatter increases (with the X-ray selected sample having a scatter 3.4 times larger than the optically selected sample). Although the scatter of the optically selected sample is lower, we find 13 optically selected GAMA groups undetected in X-rays. Inspection of the difference in magnitude between the first and second brightest galaxies in the cluster, and a stacked X-ray image of these 13 groups, suggests that these are young systems still in the process of forming.

Key words: galaxies: groups: general – X-rays: galaxies: clusters – X-rays: general.

1 INTRODUCTION

The investigation of high-mass galaxy clusters has had a rich history (e.g. LaRoque et al. 2006; von der Linden et al. 2014; Sereno &

★ E-mail: p.a.giles@sussex.ac.uk

Ettori 2015, and many others). Comparatively however, the lower-mass galaxy group population remains in largely uncharted territory, especially in the X-ray regime. A key question is the degree to which groups differ from being scaled-down versions of higher mass clusters, motivated by the expectation that non-gravitational processes [active galactic nuclei (AGNs) and supernovae feedback] are more effective in the group-scale regime. Simulations have shown that scaling relations are best modelled by an evolving broken power law (e.g. Le Brun et al. 2017; Farahi et al. 2018), highlighting the decreasing gas fraction as a function of system mass (e.g. Eckert et al. 2016, XXL Paper XIII). However, an observational consensus of the presence of a break in the scaling relations is yet to be reached, with studies showing the group scaling relations are both consistent (e.g. Sun et al. 2009) and inconsistent (e.g. Kettula et al. 2015; Lovisari, Reiprich & Schellenberger 2015) with higher mass systems. This discord remains even for studies that correct for selection effects, with Lovisari et al. (2015) and Zou et al. (2016) being inconsistent and consistent with higher mass systems respectively.

The dominance of feedback in low-mass systems should give rise to large scatter in X-ray luminosity (L_X) at fixed mass. The magnitude, and mass dependence, of this scatter provide important clues to the nature of the feedback physics. However, probing the scatter to gain insight into feedback physics is complicated due to the biases involved when selecting cluster samples. It is well known that X-ray selected cluster samples suffer from selection biases, and while recent efforts have been made to correct for these when modelling scaling relations (e.g. Stanek et al. 2006; Pacaud et al. 2007; Mantz et al. 2010; Andreon & Bergé 2012; Lovisari et al. 2015; Giles et al. 2016, 2017; Sereno et al. 2019), they may require the use of selection functions based on some prior knowledge of the range of cluster properties. Recent studies of optically selected clusters show an increased scatter in X-ray luminosity compared to X-ray selected samples (e.g. Andreon et al. 2016). Therefore, prior knowledge of the scatter used when correcting for selection effects may be incorrect, resulting in a scaling relations not fully corrected for selection biases.

Many previous attempts to compare the scaling relations of X-ray selected clusters with those of optically selected clusters have made use of samples selected on different parts of the sky and/or directly measured the scaling relations for only the X-ray or optically selected sample and relied on literature values for the comparators (e.g. Osmond & Ponman 2004; Brough et al. 2006; Andreon et al. 2016). The main drawback of these studies is that due to the different sky areas considered, direct comparisons of systems detected in the respective surveys cannot be performed. Ideally, one would perform a continuous X-ray and optical survey over the same sky area. One of the first studies study that attempts to overcome these issues, and importantly in the group regime, is Connelly et al. (2012). This work makes use of X-ray observations of two of four Canadian Network for Observational Cosmology Field Galaxy Redshift Survey 2 (CNOC2) areas, with a total area covered in X-ray observations of 0.2 and 0.3 deg^2 for the two fields, in order to compare optical groups with a sample of X-ray selected groups detected over the same area. They find consistency of the X-ray luminosity – velocity dispersion ($L_X -$ σ_v) and stellar mass – X-ray luminosity ($M_{stellar} - L_X$) relations for the X-ray and optically selected systems. However, this study was restricted to a small area (0.5 deg^2) and suffered from low redshift completeness of the X-ray selected sample.

In the present work, we extend the above approach, taking advantage of the availability on a common area of the sky of the XXL and Galaxy and Mass Assembly (GAMA) surveys. We have constructed a sample of X-ray selected clusters from the XXL survey (Pierre et al. 2016, XXL Paper I), and a sample of optically selected
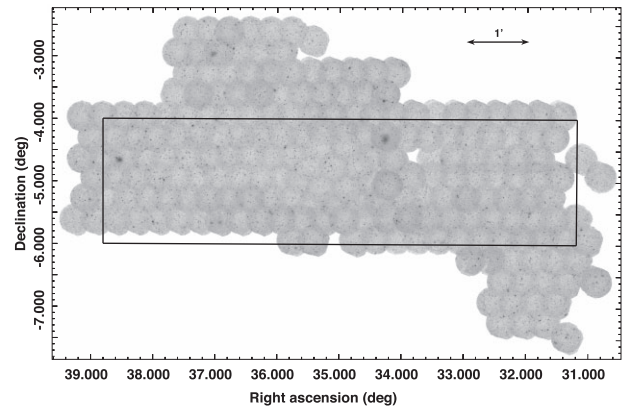

Figure 1. Count rate map of the XXL-N field (with a maximum count rate of <0.025 counts s^{-1}), the black box highlights the region used to define the XXL and GAMA selected clusters (see Section 2).

clusters from the GAMA (Driver et al. 2011) survey. By using only the overlapping region of XXL and GAMA, we will be able to make direct comparisons of the type of systems selected. The total overlap of the XXL and GAMA region covers an area of 14.6 deg^2, with a redshift completeness of 94 per cent for galaxies with $r < 19.8$.

We will investigate the form and scatter of the $L_X - \sigma_v$ between the two samples. Under the assumption of self-similarity (Kaiser 1986), one would expect the bolometric luminosity and the velocity dispersion to follow a relationship of $L_X \propto \sigma_v^4$. While many studies have observationally determined the $L_X - \sigma_v$ relation (e.g. Zhang et al. 2011; Connelly et al. 2012; Nastasi et al. 2014; Gozaliasl et al. 2020; Wetzell et al. 2021), none have taken into account the selection effects inherent when using X-ray selected samples. The well-understood selection function of XXL (Pacaud et al. 2016, hereafter XXL Paper II) is included in our analysis, which makes the XXL survey ideal for studying X-ray-based scaling relations. This will enable our measurement of the $L_X - \sigma_v$ to be free, to the best of our knowledge, from selection biases. We will compare the form and scatter of the $L_X - \sigma_v$ derived from the X-ray and optically selected samples in order to test whether the two selection methods are finding similar populations of objects, and determine how robust inferences on the scaling properties of clusters are to the selection method used.

The outline of this paper is as follows. In Section 2, we discuss the data preparation and sample selection. The X-ray and optical analysis of the sample is described in Section 3. Notes on undetected clusters during the matching process are discussed in Section 4. In Section 5, we present our results and derive the sample and bias-corrected scaling relations. Our discussion and conclusions are presented in Section 6 and Section 7, respectively. Throughout this paper, we assume a WMAP9 cosmology of $\Omega_M = 0.282$, $\Omega_\Lambda = 0.718$, and $H_0 = 69.7$ (Hinshaw et al. 2013). We use $E(z)$ to denote the redshift dependence of the Hubble parameter, given by $E^2(z) = \Omega_M(1 + z)^3 + (1 - \Omega_M - \Omega_\Lambda)(1 + z)^2 + \Omega_\Lambda$.

2 SAMPLE SELECTION

The groups/clusters used in this work were selected in the northern region of the XXL survey from the overlap between the XXL and GAMA surveys, as shown in Fig. 1 (black box). The parent X-ray sample constructed from the XXL survey and used in this work is

outlined in XXL paper II. The GAMA group catalogue (G3Cv10[1]) used in this work was derived from the GAMA DR3 release (Baldry et al. 2018), constructed via the group detection routine outlined in Robotham et al. (2011). Note that the GAMA group catalogue contains groups down to two members. We did not introduce cuts on this catalogue (other than that defined below to generate the final sample used throughout this work), however, all but one of the GAMA groups used in this work contain at least five members. The overlap region between the XXL and GAMA survey used in this work is defined by the ranges $31.2° < $ RA $ < 38.8°$ and $-6.0° < $ Dec $ < -4.0°$, totalling 14.6 deg^2 (excluding *XMM* observations significantly effected by flaring, and areas not covered by the *XMM* observations due to the choice of a crude box selection). Note that the GAMA survey extends to lower declination in the XXL field, but the spectroscopic completeness of the survey drops significantly below $-6°$. In this region, we were able to define X-ray and optically selected cluster samples of approximately equal size. For brevity, we henceforth use the term clusters throughout to refer to both groups and clusters of galaxies.

The X-ray detection of clusters within XXL is outlined in XXL paper II, and we briefly review their selection criteria here. Sources are classed as extended if their measured extent is larger than 5 arcsec and their extent likelihood is larger than 15. Extended sources are then separated into two classes, the C1 class with extent likelihood larger than 33 and detection likelihood larger than 32, and the C2 class with an extent likelihood between 15 and 33 (with no limits on the detection likelihood). Our simulations of the selection function demonstrate that the C1 class represents a nearly 100 per cent pure selection of clusters, while the C2 class should have a purity of about 50 per cent. For this analysis, we selected all C1 clusters in the XXL/GAMA overlap region and within a redshift range of $0.05 < z < 0.3$. This redshift limit was chosen as a trade off between providing a large sample size, and be similar to the redshift limit used to select the GAMA cluster sample (see below). Using the conditions outlined above, the C1 sample contained 38 clusters. Next, we matched to GAMA clusters by finding all GAMA clusters within 3 arcmin of an XXL C1 cluster, and visually inspected these matches for the GAMA cluster associated with the C1 selected clusters. Note that no redshift cut was implicitly added to the matching since the GAMA survey was used as a redshift source for the XXL survey (see Adami et al. 2018, hereafter XXL Paper XX). All C1 clusters matched to a GAMA cluster had a redshift difference of <2 per cent. Our final X-ray selected sample with matched GAMA clusters consists of 34 clusters, representing a 90 per cent complete sample. We found four C1 clusters without a corresponding GAMA detection, these clusters are individually discussed in Section 4.1. Based on the inspection of the X-ray and optical data, three of the C1 clusters without an associated GAMA cluster was due to possible merging activity. From the X-ray emission, two nearby X-ray extended sources have been detected as separate X-ray detections, whereas the GAMA routine has determined the galaxies belong to one system (typically associated with the higher flux X-ray cluster). The remaining C1 cluster without a GAMA detection remains unresolved as to the nature of why it is undetected in GAMA. Note that for the C1 XXL sample, redshifts are taken from XXL Paper XX, making use of the increased spectroscopic follow-up of XXL clusters (as opposed to using just GAMA catalogue redshifts).

The GAMA selected sample was chosen within the same region and to have a minimum group optical luminosity (in the r-band) of

$L_{opt} > 1.18 \times 10^{11}$ L$_\odot$ (see Section 3.2 for details of how the total group luminosity was calculated). Due to the selection of GAMA clusters in L_{opt}, the Malmquist bias in the resulting X-ray luminosity–σ_v relation due to the GAMA selection is negligible (only due to any correlation between L_{opt} and σ_v). We employed an additional redshift limit of $z < 0.2$ on the GAMA selection since the estimate of the group luminosity has a greater level of bias above a redshift of 0.2 (see fig. 10 in Robotham et al. 2011). The choice of the luminosity limit was driven to provide a comparable sample size to the C1 XXL sample defined above. This resulted in a GAMA sample consisting of 28 optically selected clusters. We then performed a matching process to the XXL C1 and C2 catalogue to associate these GAMA clusters with XXL sources. Briefly, we used the GAMA defined centroid (see Section 3.2) to match to XXL sources. From this centroid position, we found all XXL C1 and C2 clusters within 3 arcmin and visually inspected these matches to confirm the association. This resulted in 15 GAMA clusters matched with a C1 or C2 XXL cluster. We therefore found that the GAMA selected sample is only 54 per cent complete in X-ray detection. The remaining 13 clusters did not match to a C1 or C2 XXL cluster and we label these as 'undetected'. Note that some of these clusters have an X-ray source associated with them but fell outside our C1 and C2 detection criteria. See Section 4.2 for discussions on individual 'undetected' clusters. Redshifts for the GAMA selected sample were taken from XXL Paper XX if matched to an XXL cluster. For GAMA clusters without an XXL match, redshift were taken from the group catalogue.

The samples of clusters are illustrated in Fig. 2, plotted in the plane of X-ray luminosity and redshift. X-ray luminosities are measured in the (0.5–2) keV band and extrapolated out to r_{500} (based upon the measurement within 300 kpc, as detailed in Section 3). The large number of GAMA clusters at $z \approx 0.14$ is related to a large-scale structure in the XXL field (two superclusters were discovered at this redshift in XXL Paper XX). A similar feature is also apparent in GAMA DR3 (see fig. 6 in Baldry et al. 2018).

3 CLUSTER ANALYSIS

Here, we describe the cluster analysis process used in this work, first describing the X-ray analysis, followed by a brief review of the optical analysis of the clusters (as fully described in Robotham et al. 2011).

3.1 X-ray analysis

The main goal of the X-ray analysis is to measure the X-ray luminosity of each cluster. For all of the C1 clusters and any GAMA-selected clusters with bright enough X-ray counterparts, a standard X-ray spectroscopic analysis was performed, centred on the X-ray centroid. For the 13 GAMA-selected clusters without a matched C1 or C2 X-ray source, a simpler aperture photometry approach was used to estimate the X-ray luminosity (with four of these GAMA systems only having an upper limit X-ray luminosity estimated). For these clusters, the analysis was centred on the GAMA defined iterative centroid. The two X-ray analysis methods are described below.

3.1.1 Spectral analysis

Many of the clusters in the XXL region are considered to be in the low X-ray count regime and therefore the treatment of the background is critical. The first step of our analysis was to determine
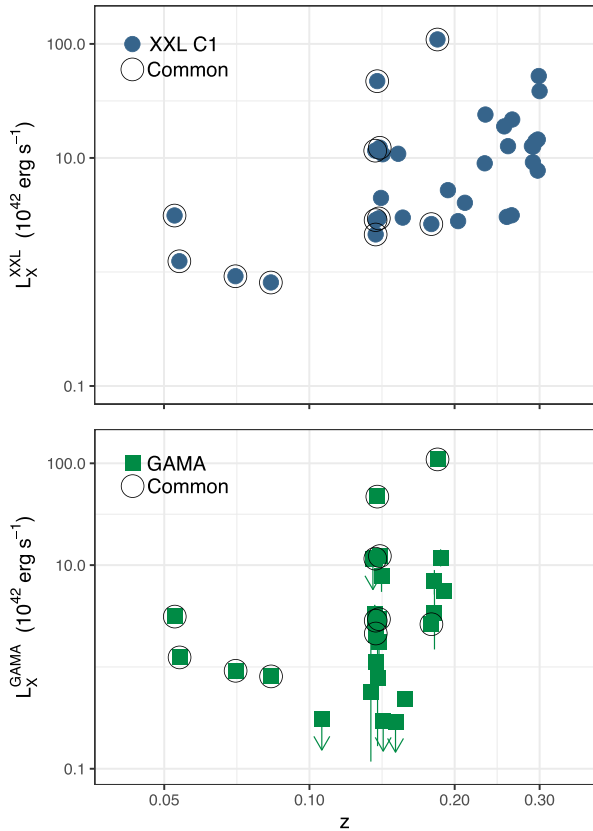
---

[1] http://www.gama-survey.org/dr3/data/cat/GroupFinding/v10/

Figure 2. The X-ray luminosity-redshift plane of the XXL (light blue circles, top plot) and GAMA (green squares, bottom plot) cluster samples defined in Section 2. Clusters that appear in both samples are highlighted by the black circles. Points with downward arrows in the GAMA sample represent upper limits. L_X^{XXL} and L_X^{GAMA} denotes the X-ray luminosity in the (0.5–2) keV band within r_{500} for the XXL and GAMA sample, respectively.

the radial extent of the cluster emission so that the background may be measured in a region free from cluster emission. A radial surface brightness profile of the cluster was first extracted from each of the EPIC detectors (PN, MOS1, and MOS2), and then summed. The background level in the profile was then modelled by a flat (particle) and vignetted (X-ray) component. These two model components were fit to the outer parts of the surface brightness profile (excluding the central 250 arcsec) in order to constrain the background level. Based on this background level, the extent of the cluster emission was estimated as the radius beyond which no emission was detected at a significance of $>0.5\sigma$ above the background. The background levels are then refitted to the radial profile with the cluster emission excluded out to this detection radius, and the cluster extent is estimated once more. This was repeated until the cluster extent changed by less than 1 per cent. This is a conservative approach to ensure that no significant cluster emission is included in the region used to determine the background in our spectral fitting.

In order to account for the background in the spectral analysis, we perform a detailed modelling of the background instead of a simple background subtraction. This method requires the modelling of all the various background components, and followed closely the method outlined in Eckert et al. (2014). We briefly describe the modelling of each component below:

(i) *The non X-ray background (NXB)*: closed-filter observations were used to estimate the NXB, modelled using a phenomenological model. This was then used as an additive component in the spectral modelling. The normalization of the NXB and prominent background lines were left free during the fitting process to allow for systematic variations. For observations contaminated by soft protons, where the ratio of the count rate measured inside the field of view (FOV) but at off-axis angles beyond 10 arcmin, and the count rate measured in the out-of-FOV regions of the detector was >1.15 (Leccardi & Molendi 2008), we included an additional broken power-law component, with the slopes fixed at 0.4 and 0.8 below and above 5 keV, respectively.

(ii) *The sky background*: for each cluster, an offset region free from cluster emission (outside the extent radius determined above) was chosen to model the sky background. A three-component model was used to model the sky background. To model the X-ray background, we used a power law with photon index fixed at 1.46. The local hot bubble was modelled using an unabsorbed thermal component at 0.11 keV. Lastly, the Galactic halo emission was modelled with a thermal component at 0.22 keV. The model was included in the source spectrum, re-scaled by the ratio of the areas, accounting for CCD gaps and bad pixels.

Cluster source spectra were extracted for each of the *XMM* EPIC cameras in an aperture of radius 300 kpc and fits were performed in the 0.4–11.0 keV band with an absorbed APEC (Smith et al. 2001) model (v2.0.2) with the absorbing column fixed at the Galactic value (Kalberla et al. 2005). The spectra for each camera were fit simultaneously with the temperature of the APEC components tied together. The fits were performed using XSPEC (v12.8.1i) and the abundance table from Anders & Grevesse (1989). Due to the low number of counts for many of the clusters, the spectra were fitted using the cstat statistic, with the background cluster spectra grouped to contain at least five counts per bin and this grouping applied to the source spectra (Pacaud et al. 2006). Throughout the spectral analysis, we assumed a fixed metal abundance of 0.3 solar. The normalizations for each camera were free to vary in the spectral fit, with the PN camera used to calculate the X-ray luminosity in the (0.5–2) keV band.

As per the method in Giles et al. (2016, hereafter XXL Paper III), the luminosities calculated above, within 300 kpc, were extrapolated out to a radius of r_{500} (the radius enclosing a mean density of 500 times the critical density at the cluster redshift). The extrapolation assumes that the X-ray surface brightness follows a β-profile with $r_c = 0.15r_{500}$ and $\beta = 0.667$. The r_{500} values for each cluster were derived from their velocity dispersion using the correlation between mass and σ_v (the $M - \sigma_v$ relation; see Section 5.1). The β-profile parameters were chosen to match those adopted in XXL paper II, used for the modelling of the selection function. We note that the uncertainties on the luminosity are scaled by this extrapolation, but do not include any uncertainty on the β-profile parameters.

3.1.2 Aperture photometry analysis

The following method was used for the 13 optically selected clusters that were not matched to either a C1 or C2 XXL X-ray cluster. These cases either have no significant X-ray emission (e.g. Group ID 400076, Section 4.2.9), or the detected X-ray emission fell outside the classification limits of a C1 or C2 cluster (e.g. Group ID 400027, Section 4.2.4). See Section 4.2 for discussions on individual 'undetected' clusters. In all cases, the signal to noise was too low to permit a spectroscopic X-ray analysis (as described in Section 3.1). Therefore, we used the X-ray aperture photometry method based on a Bayesian

approach, fully described in Willis et al. (2018). Briefly, photon counts and exposure time information are extracted for the source and background apertures and used to estimate the background-marginalized posterior probability distribution function of the source count-rate. We assumed Poisson likelihoods for the detected number of source counts and background counts. The mode of the posterior probability function is determined, and the lower and upper bounds are given by the 68 per cent confidence region. When the mode is equal to zero, only the upper confidence bound is evaluated, and it is considered as an upper limit. Out of the 13 clusters analysed using this method, 4 were found to have count rate upper limits.

For each of the 13 clusters, we extracted PN count-rates in the (0.5–2) keV energy band within a 300 kpc aperture centred at the position of the GAMA cluster. The background aperture is either taken from a detached annulus centred around the cluster position, if the cluster is close enough to the pointing centre (<2 acmin), or from an annular sector encompassing and avoiding the cluster aperture at similar off-axis angle. An energy conversion factor (ECF) is used to obtain the corresponding cluster luminosity. The ECF for each cluster was obtained by constructing a fake spectra using XSPEC based upon an absorbed APEC model. For each cluster, we assumed a Galactic absorbing column determined at the GAMA centroid position, the redshift fixed at the GAMA spectroscopic redshift, a fixed abundance of 0.3 $Z_\odot$ and a fixed temperature of 3 keV. The fake spectrum used an Auxiliary Response File (ARF) and Redistribution Matrix File (RMF) extracted within a 300 kpc region centred on the GAMA defined centroid. The ECF was then estimated by dividing the flux calculated in the 0.5–2.0 keV band by the modelled count rate. The count rates from the aperture photometry method was multiplied by the ECF to convert to a flux, and this flux converted to a luminosity. Once again, this 300 kpc luminosity was extrapolated out to r_{500} by integrating under a β-profile (see Section 3.1.1).

3.2 Optical analysis

The GAMA clusters were selected based on the total group optical luminosity and a redshift of z<0.2. Full details of the group luminosity estimator can be found in Robotham et al. (2011, section 4.4 of the paper). Briefly, the absolute magnitude limit of each group was calculated and the r_{AB}-band luminosity was measured within this limit. This was then integrated to a nominal faint limit using the global GAMA galaxy luminosity function in order to correct for the missing flux. For each group, the following is calculated

$$L_{opt} = B L_{ob} \frac{\int_{-30}^{-14} 10^{-0.4 M_r} \phi_{GAMA}(M_r) \mathrm{d}M_r}{\int_{-30}^{M_{r-lim}} 10^{-0.4 M_r} \phi_{GAMA}(M_r) \mathrm{d}M_r} \quad (1)$$

where L_{ob} is the total observed r_{AB}-band luminosity of the group, B is the scaling factor required to produce a perfectly median unbiased luminosity estimate, and M_{r-lim} is the effective r_{AB}-band absolute magnitude limit for the group.

The determination of the velocity dispersions used throughout this work is briefly described below, with full details given in Robotham et al. (2011, section 4.1 of the paper). The group velocity dispersion was measured using the *gapper* method (as detailed in Beers, Flynn & Gebhardt 1990). For a group multiplicity of N, recession velocities are ordered within the group and gaps between each velocity pair are calculated using $g_i = v_{i+1} - v_i$ and for $i = 1, 2, 3,.., N-1$, as well as weights defined as $w_i = i(N-i)$. The velocity dispersion is estimated via

$$\sigma_v = \frac{\sqrt{\pi}}{N(N-1)} \sum_{i=1}^{N-1} w_i g_i. \quad (2)$$

The resulting σ_v was then multiplied by a further factor of $\sqrt{N/(N-1)}$. This corrects for the fact that the brightest galaxy tends to move with the halo centre of mass, and was calibrated by the analysis of simulated haloes (see Robotham et al. 2011, section 2.3 of the paper for further details).

Finally, we used the GAMA defined centroid during our matching processes (see Section 2). The centroid was defined through an iterative procedure, whereby in each step the r_{AB}-band centre of light was defined and the most distant galaxy rejected. The process was repeated until two galaxies remained, and the brighter galaxy used as the group centre.

4 UNDETECTED CLUSTERS DURING THE MATCHING PROCESS

4.1 XXL C1 clusters unmatched in GAMA

As found in Section 2, there are four clusters in the X-ray C1 sample that do not have a corresponding GAMA cluster associated with them. Here, we discuss each of these clusters, highlighting potential reasons for a lack of a GAMA match. Figs 3(a)–(d) show *XMM* images of these systems. In each case, the X-ray images have been smoothed by a Gaussian of width 3.3 arcsec (note for the purposes of these images, they have not been background subtracted). The circles represent the positions of member galaxies detected in the GAMA survey. The red circle represents the group centroid determined galaxy. The size of each image was chosen to enclose all group galaxies.

4.1.1 XLSSC 022

The cluster XLSSC 022, z = 0.293 (Fig. 3a), is matched to a GAMA group with only three members. The red circle highlights the GAMA defined central galaxy for the match group (coincident with the peak of the cluster emission), with the two other group galaxies highlighted in blue. There is a nearby cluster (XLSSC 027, distance ~1500 kpc) at the same redshift as XLSSC 022, which belongs to the C1 sample used in this work. It is unclear why XLSSC 022 (as the higher flux cluster) has only three GAMA members.

4.1.2 XLSSC 117

The cluster XLSSC 117, z = 0.298 (Fig. 3b), again has GAMA galaxies coincident with its X-ray emission; however, they are determined to be members of the GAMA group 400004 (with 40 members), matched to the C1 cluster XLSSC 111. Since XLSSC 117 and 111 are at the same redshift, it is indeed possible that 117 is a sub-clump of the higher flux 111 cluster. Due to the association of the galaxies with XLSSC 111, we drop XLSSC 117 from the C1 sample.

4.1.3 XLSSC 151

The cluster XLSSC 151, z = 0.189 (Fig. 3c), has no corresponding GAMA matched cluster. The X-ray detection of the cluster appears to have embedded point source emission and is nearby a low surface brightness cluster. The nearby extended X-ray emission is not detected as an extended source in the XXL catalogue; however, there appears to be a GAMA group with 12 members (z = 0.28) coincident with the extended emission.
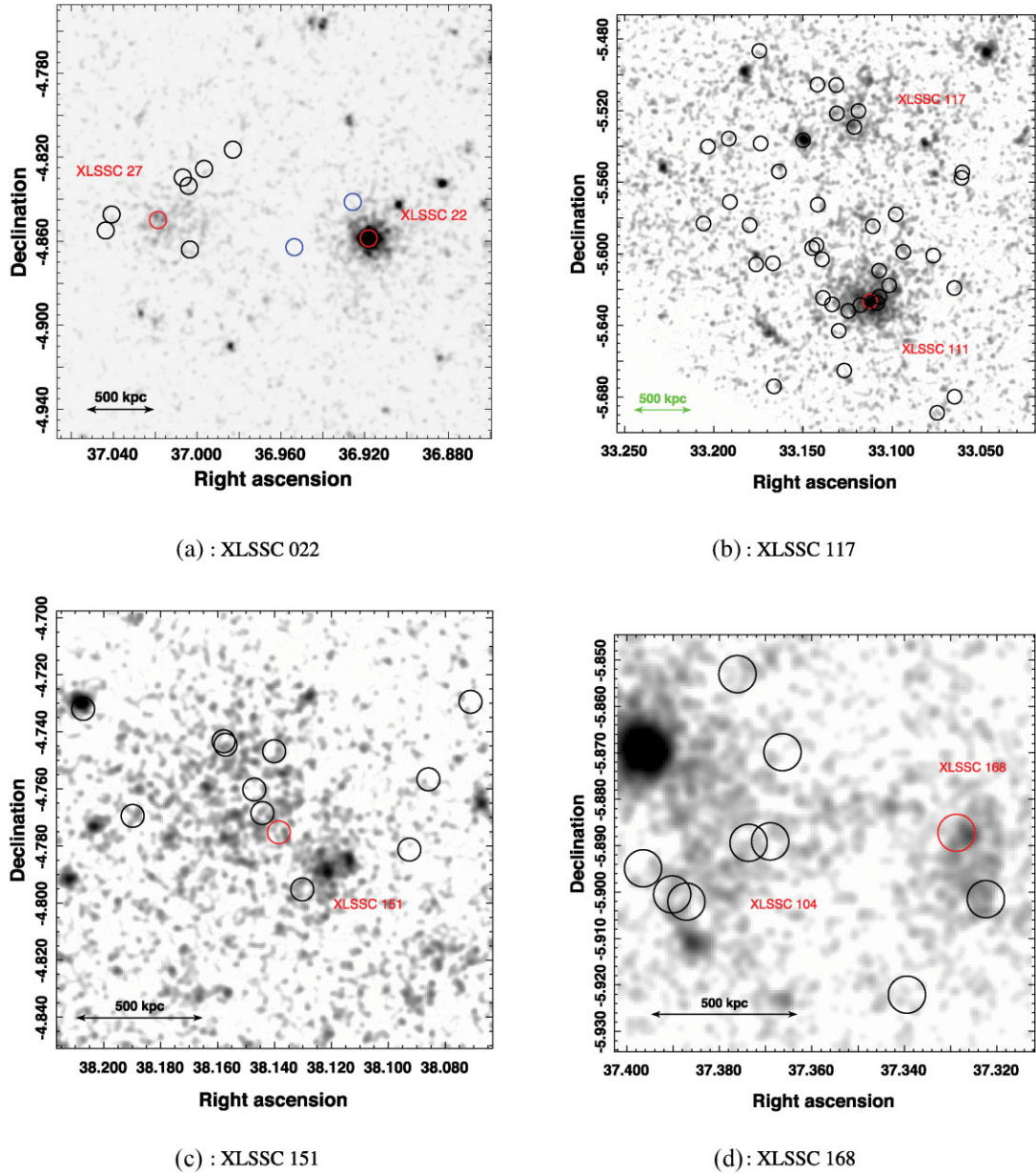
(a) : XLSSC 022

(b) : XLSSC 117

(c) : XLSSC 151

(d) : XLSSC 168

Figure 3. Smoothed raw X-ray images of C1 clusters without a corresponding GAMA group. In each case, the image covers the 0.5–2.0 keV band smoothed by a Guassian of with 3.3 arcsec. The circles represents the position of member galaxies and the red circle highlights the iterative centroid galaxy (see Section 3.2).

4.1.4 XLSSC 168

The cluster XLSSC 168, z = 0.295 (Fig. 3d), has GAMA galaxies coincident with its X-ray emission; however, it was determined that the GAMA group was matched to the C1 cluster XLSSC 104 (all galaxies in Fig. 3(d) belong to only one GAMA defined group). This was determined based upon the distribution of member galaxies with the more extended C1 cluster. Therefore, XLSSC 168 is dropped from the C1 sample.

4.2 GAMA clusters unmatched in XXL

As found in Section 2, 13 GAMA groups are not associated with significant extended X-ray emission based (by this we mean

not associated with a C1 or C2 defined source) on the XXL observations. For each of these clusters, the analysis of the X-ray data to determine the luminosity was performed using an aperture photometry method (see Section 3.1.2). Here, we discuss each of these clusters in detail, highlighting possible reasons for the lack of X-ray emission. In each case, the cluster is identified by its six-digit GAMA Group ID. While it is difficult to attribute an astrophysical reason as to why these clusters are unmatched to an XXL C1/C2 source due to observational reasons (e.g. six of the GAMA clusters fall at an off-axis position >10 arcmin from the aimpoint, making detection difficult due to the lower sensitivity), these clusters are discussed further in Section 6.3. Fig. 4(a–m) shows *XMM* images of these systems (see Section 4.1 for description).
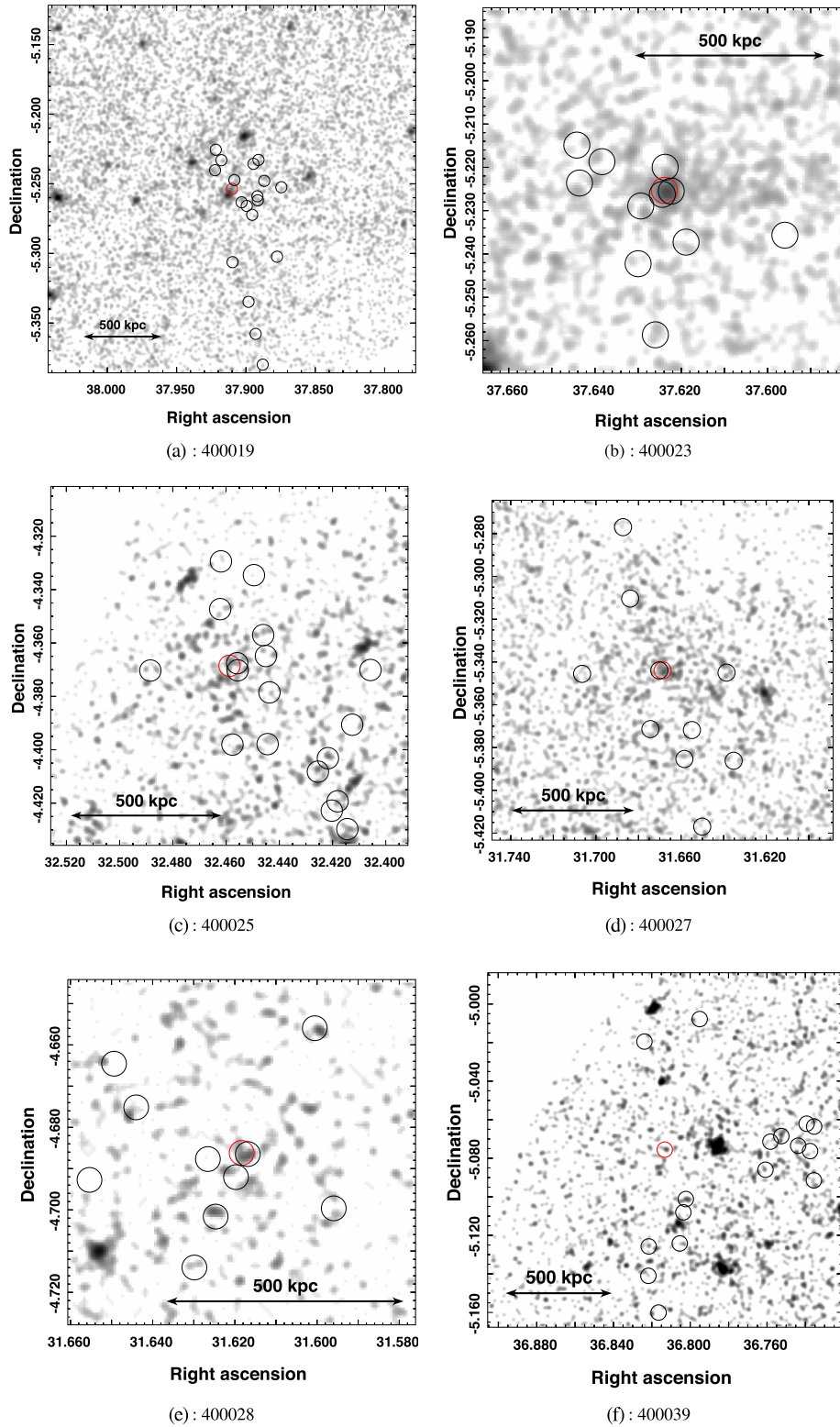
(a) : 400019

(b) : 400023

(c) : 400025

(d) : 400027

(e) : 400028

(f) : 400039

Figure 4. Smoothed raw X-ray images of undetected GAMA clusters. In each case, the image covers the 0.5–2.0 keV band smoothed by a Guassian of with 1.5σ. The circles representthe position of member galaxies and the red circle highlights the iterative centroid galaxy (see Section 3.2).
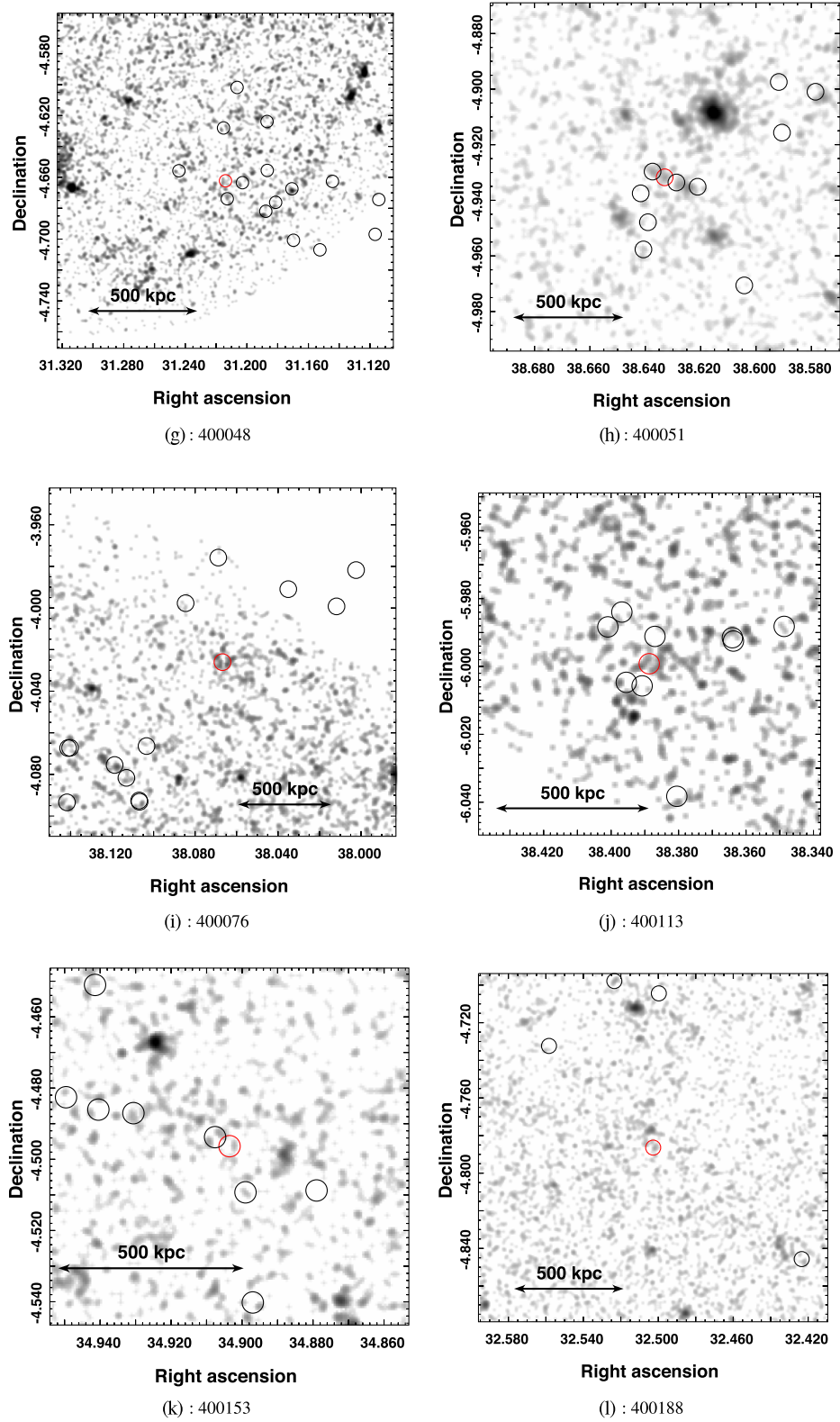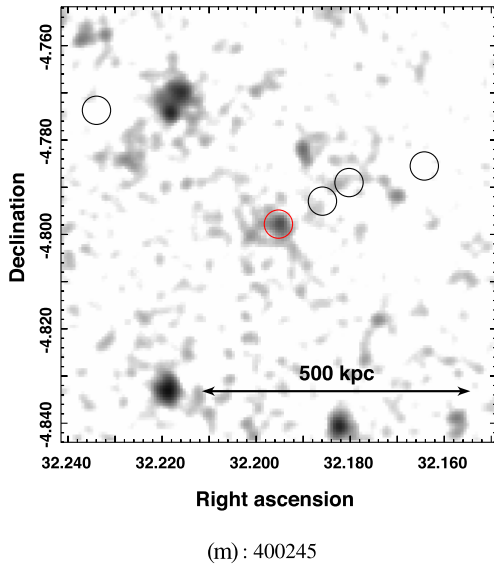
(g) : 400048

(h) : 400051

(i) : 400076

(j) : 400113

(k) : 400153

(l) : 400188

Figure 4. *– continued*

(m) : 400245

Figure 4. – *continued*

4.2.1 400019

The cluster 400019 (see Fig. 4a) lies at ≈ 8 arcmin off-axis in the *XMM* pointing. The cluster flux was determined using the aperture photometry method. The effective exposure time at the position of the GAMA centroid is 7 ks.

4.2.2 400023

The cluster 400023 is shown in Fig. 4(b). There is an XXL source coincident with the GAMA cluster; however the X-ray source falls just outside the criteria for being classed as a C2 cluster, with an extent likelihood of 29.6 and an extent of 4.4 arcsec (with C2 clusters having an extent ≥ 5 arcsec).

4.2.3 400025

The cluster 400025 (Fig. 4c) appears at an off-axis position of 12.7 arcmin in the *XMM* observation. The lower effective area and large PSF at this off-axis position is the most likely cause of a lack of significant cluster emission detected. Furthermore, at this position, the effective exposure time of the PN camera is just 0.7 ks.

4.2.4 400027

The cluster 400027 is shown in Fig. 4(d). There is a detected X-ray source at the position of the GAMA cluster BCG; however, the extent likelihood of the X-ray source is 8.13 (with C2 clusters having an extent likelihood of $15 < \text{EXT\_LH} < 32$). We note that the source falls on the broken MOS1 chip, likely effecting it's detectability.

4.2.5 400028

The cluster 400028 (Fig. 4e) appears at an off-axis position of 10.3 arcmin in the *XMM* observation. The lower effective area and large PSF at this large off-axis position is the most likely cause of a lack of significant cluster emission.

4.2.6 400039

The cluster 400039 (Fig. 4f) appears at an off-axis position of 12.4 arcmin in the *XMM* observation. The lower effective area and large PSF at this large off-axis position is the most likely cause of a lack of significant cluster emission.

4.2.7 400048

The cluster 400048 (Fig. 4g) appears at an off-axis position of 10.1 arcmin in the *XMM* observation, and close to the edge of the PN FOV. The lower effective area and large PSF at this large off-axis position is the most likely cause of a lack of significant cluster emission.

4.2.8 400051

The cluster 400051 (Fig. 4h) has an XXL source associated with the iterative centroid galaxy in GAMA. The source has an extent of 5.9 arcsec (above the C2 threshold), however the extent likelihood is only 4.6, below the C2 cut-off of 15. Unfortunately, the observation suffered from flaring and the exposure times of the observation after cleaning were 3.8, 7.9, and 8.6 ks for the PN, MOS1, and MOS2 cameras, respectively. Based on the number of counts from the aperture photometry method, the nominal XXL exposure time of 10 ks would have resulted in a robust detection with >150 cluster counts, improving the reliability of the extent measurement.

4.2.9 400076

The cluster 400076 (Fig. 4i) shows an interesting morphology in terms of the individual galaxies. The galaxies appear to be separated into two groups on the sky, one group to the south-west and one to the north-east, and separated by roughly 1 Mpc on the sky. This suggests that the cluster may be still in the process of forming, with the lack of X-ray emission due to the gas not yet heated to virial temperatures. However, due to its large off-axis position in the *XMM* image (at 10.5 arcmin), and that the cluster falls on the broken MOS1 chip, detection of cluster emission remains challenging.

4.2.10 400113

The source 400113 (see Fig. 4j) is a poor system with 10 galaxy members, and appears at an off-axis position of 13 arcsec in the *XMM* observation. The lower effective area and large PSF at this large off-axis position is the most likely cause of a lack of significant cluster emission.

4.2.11 400153

The XXL observation for the cluster 400153 (see Fig. 4k), suffered from flaring, resulting in approximately 4, 3, and 6 ks of good time for the PN, MOS1, and MOS2 cameras, respectively.

4.2.12 400188

The source 400188 (see Fig. 4l) appears to be a very poor system (with only five members from GAMA) spread over a large area. The luminosity was estimated via the aperture photomtry method, and the cluster represents the largest outlier in the $L_X^{GAMA} - \sigma_v$ relation. Therefore, it's σ_v appears to be overestimated due to the small number of members.

Table 1. Properties of the X-ray selected C1 cluster sample.

XLSSC Num	GAMA ID	z	N_{fof}	σ_v km s^{-1}	$r_{500,\,M\sigma}$ Mpc	L_X^{XXL} 10^{42} (ergs s^{-1})	Δ_{m12}
XLSSC 011*	400026	0.054	42	357 ± 32	587	1.23 ± 0.11	0.63
XLSSC 022	–	0.293	–	–	–	–	–
XLSSC 025	400119	0.265	7	616 ± 40	676	21.79 ± 1.78	1.12
XLSSC 027	400108	0.295	8	497 ± 36	603	14.48 ± 1.32	0.03
XLSSC 021*	400054	0.085	9	306 ± 38	540	0.80 ± 0.08	0.95
XLSSC 041	400221	0.142	9	385 ± 44	583	10.70 ± 0.93	1.47
XLSSC 044	400049	0.263	11	362 ± 46	533	3.12 ± 0.42	0.01
XLSSC 054*	400003	0.054	54	414 ± 39	627	3.11 ± 0.20	0.79
XLSSC 055	400007	0.232	19	656 ± 45	706	24.13 ± 1.65	0.69
XLSSC 057	400013	0.153	20	467 ± 38	631	10.84 ± 0.89	0.69
XLSSC 060*	400001	0.139	97	661 ± 46	742	47.41 ± 1.25	0.82
XLSSC 061	400020	0.259	14	408 ± 58	563	12.62 ± 1.53	0.82
XLSSC 075	400138	0.211	6	222 ± 43	441	3.99 ± 0.40	0.26
XLSSC 087	400164	0.141	11	276 ± 41	503	12.16 ± 1.06	1.09
XLSSC 088	400109	0.295	9	688 ± 38	698	14.10 ± 1.74	0.04
XLSSC 090	400073	0.141	9	355 ± 40	562	4.43 ± 0.48	1.68
XLSSC 091*	400002	0.186	59	1121 ± 52	918	111.93 ± 3.32	0.41
XLSSC 095*	400134	0.138	9	359 ± 30	566	2.12 ± 0.28	0.74
XLSSC 103	400101	0.233	8	246 ± 45	456	8.87 ± 1.03	0.07
XLSSC 104	400050	0.294	10	557 ± 50	636	9.18 ± 1.23	0.04
XLSSC 106	400008	0.300	23	657 ± 44	682	38.72 ± 2.07	0.42
XLSSC 108	400047	0.254	10	306 ± 40	497	18.75 ± 1.75	1.11
XLSSC 111	400004	0.300	41	752 ± 41	724	52.69 ± 4.13	0.10
XLSSC 112*	400015	0.139	17	477 ± 47	642	2.85 ± 0.16	1.23
XLSSC 117	–	0.298	–	–	–	–	–
XLSSC 123	400016	0.194	15	463 ± 44	616	5.20 ± 0.76	0.85
XLSSC 146	400055	0.254	14	418 ± 44	570	3.03 ± 0.45	0.24
XLSSC 150	400010	0.292	16	663 ± 45	688	12.62 ± 1.84	0.78
XLSSC 151	–	0.189	–	–	–	–	–
XLSSC 154*	400075	0.179	8	489 ± 43	636	2.63 ± 0.15	0.99
XLSSC 166	400156	0.158	7	552 ± 40	679	3.00 ± 0.38	1.96
XLSSC 167	400435	0.298	4	251 ± 47	444	7.67 ± 1.14	0.15
XLSSC 168	–	0.295	–	–	–	–	–
XLSSC 176	400187	0.141	8	316 ± 38	534	2.93 ± 0.41	0.72
XLSSC 180	400021	0.289	13	973 ± 41	817	12.90 ± 0.82	0.85
XLSSC 189	400173	0.204	5	377 ± 50	560	2.77 ± 0.38	0.72
XLSSC 190*	400041	0.070	32	285 ± 40	527	0.91 ± 0.05	0.34
XLSSC 201*	400012	0.138	23	598 ± 38	710	11.62 ± 1.56	0.82

* denotes clusters that are in common with the GAMA selected sample. C1 clusters not matched to a GAMA group have no corresponding GAMA ID (and hence no optical or X-ray properties are listed). Redshifts are taken from XXL Paper XX.

4.2.13 400245

The cluster 400245 is shown in Fig. 4(m). There is a source associated with the galaxy defined as the iterative centroid; however, the XXL source detection routine classifies the source as point-like, with an extent likelihood of 54.2 and an extent of 3.4 arcsec (with C1 clusters having and extent ≥5 arcsec). Since this is classed as a point source and one cannot exclude the possibility the emission is coming from an AGN, the source is excluded in our aperture photometry method.

5 RESULTS

The X-ray and optical properties of the XXL and GAMA selected samples are given in Tables 1 and 2, respectively.

In the following sections, we first briefly present the measurement of the $M - \sigma_v$ relation used to estimate r_{500} values for the clusters and also as a part of our bias correction of the $L_X - \sigma_v$ relation. We then present measurements of the scaling of X-ray luminosity and velocity dispersion, both without correction for selection biases

and including a model of the XXL selection function. We note that we assume that the optical selection is free from selection effects in the current analysis (leaving further optical selection correction for future analysis), and focus only on X-ray selection biases. In order to simplify notation, we refer the soft band luminosity extrapolated out to r_{500} using the $M - \sigma_v$ relation, as L_X^{XXL} and L_X^{GAMA} for the XXL and GAMA selected sample, respectively.

5.1 The $M - \sigma_v$ relation

An $M - \sigma_v$ relation is needed for both the calculation of r_{500} and to convert the mass function to a σ_v function (see Section 5.3) for the bias correction of the $L_X - \sigma_v$ relation. Our $M - \sigma_v$ relation is derived using the XXL selected sample (see Section 2 and Table 1), with masses taken from Umetsu et al. (2020, $M_{500,\,MT}$ in table 2). Note that not all clusters in Umetsu et al. (2020) have a measured mass, therefore limiting our sample to 31 (of the available 34) clusters used to constrain the $M_{WL} - \sigma_v$ relation.

Table 2. Properties of the optically selected cluster sample. Clusters with no XLSSC number represent GAMA clusters with no significant X-ray emission and their X-ray properties determined using the aperture photometry method (see Section 3.1.2).

XLSSC Num	GAMA ID	z	N_{fof}	σ_v km s^{-1}	$r_{500, M\sigma}$ Mpc	L_X^{GAMA} 10^{42} (ergs s^{-1})	Δ_{m12}
XLSSC 011*	400026	0.054	42	357 ± 32	751	1.25 ± 0.15	0.63
XLSSC 021*	400054	0.085	9	306 ± 38	699	0.81 ± 0.08	0.95
XLSSC 054*	400003	0.054	54	414 ± 39	799	3.14 ± 0.20	0.79
XLSSC 060*	400001	0.139	97	661 ± 46	958	47.39 ± 1.25	0.82
XLSSC 074	400106	0.192	9	278 ± 47	661	5.51 ± 0.75	1.01
XLSSC 087*	400164	0.141	11	276 ± 41	663	12.35 ± 1.07	1.09
XLSSC 091*	400002	0.186	59	1121 ± 52	1191	109.98 ± 3.26	0.41
XLSSC 095*	400061	0.138	10	267 ± 33	655	2.06 ± 0.27	0.45
XLSSC 112*	400015	0.139	17	477 ± 47	834	2.87 ± 0.17	1.23
XLSSC 119	400037	0.158	10	245 ± 45	628	0.49 ± 0.03	1.67
XLSSC 154*	400075	0.179	8	489 ± 43	838	2.64 ± 0.15	0.99
XLSSC 162	400060	0.138	8	202 ± 36	583	1.11 ± 0.07	0.89
XLSSC 176*	400187	0.141	8	316 ± 38	701	2.97 ± 0.42	0.72
XLSSC 190*	400041	0.070	32	285 ± 40	680	0.92 ± 0.05	0.34
XLSSC 201*	400012	0.138	23	598 ± 38	921	11.65 ± 1.56	0.82
–	400019	0.141	19	238 ± 38	623	$7.83^{+2.46}_{-2.35}$	0.12
–	400023	0.187	12	490 ± 53	839	$11.89^{+2.42}_{-2.16}$	0.94
–	400025	0.138	19	277 ± 42	664	$0.78^{+2.98}_{-0.61}$	0.02
–	400027	0.137	11	467 ± 47	829	$3.33^{+0.76}_{-0.71}$	1.08
–	400028	0.135	11	251 ± 27	638	<11.53	0.01
–	400039	0.142	17	225 ± 30	608	<0.30	1.02
–	400048	0.106	16	146 ± 29	509	<0.31	0.38
–	400051	0.139	11	352 ± 38	735	$1.76^{+0.99}_{-0.84}$	0.04
–	400076	0.182	14	269 ± 36	651	$6.94^{+2.02}_{-1.79}$	1.39
–	400113	0.182	10	586 ± 35	906	$3.36^{+2.40}_{-1.87}$	0.30
–	400153	0.151	9	216 ± 36	597	<0.29	0.19
–	400188	0.134	5	595 ± 28	919	$0.57^{+1.97}_{-0.45}$	0.93
–	400245	0.137	5	456 ± 34	820	$2.89^{+1.10}_{-1.04}$	0.12

* denotes clusters in common with the XXL selected sample. Clusters without X-ray luminosity uncertainties indicate upper limits. Redshifts for clusters with an XXL match are taken from XXL Paper XX, those without an XXL match have their redshifts taken from the group catalogue.
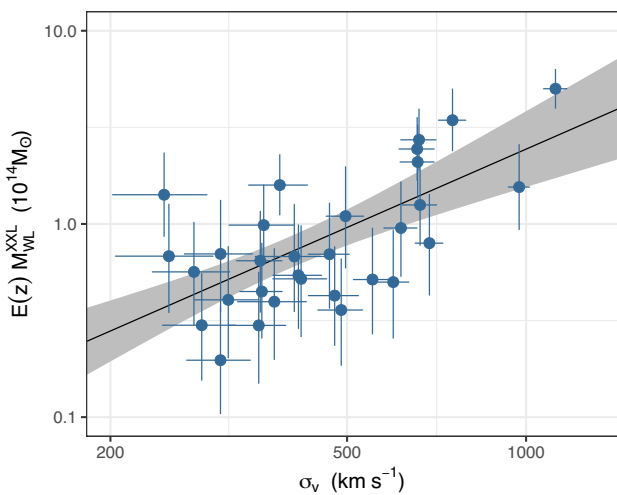

Figure 5. $M_{WL} - \sigma_v$ relation of a subset (see Section 5.1) of XXL clusters in the GAMA/XXL overlap region. The masses are adopted from Umetsu et al. (2020). The best fit to the data (assuming equation 3) is given by the black line, with the grey shaded region highlighting the 1σ uncertainty.

The $M_{WL} - \sigma_v$ relation was fitted with a power law of the form

$$\left(\frac{M_{WL}}{M_0} \right) E(z)^{\gamma_{M\sigma}} = A_{M\sigma} \left(\frac{\sigma}{\sigma_0} \right)^{B_{M\sigma}}. \tag{3}$$

The model was fitted to the data using the LINEAR REGRESSION IN ASTRONOMY (LIRA; Sereno 2016) package,[2] performed in base-ten log space and assuming self-similar evolution ($\gamma_{M\sigma} = 1$). The priors on the parameters were chosen following Sereno & Ettori (2015). For the intercept and the mean of the covariate distribution, we adopted a uniform distribution. For the variances, we adopted an inverse Gamma distribution. For the slopes, we adopted the Student's t_1 distribution with one degree of freedom, as suitable for uniformly distributed direction angles. The intrinsic scatter of the data about the relation is modelled in LIRA as a lognormal distribution with standard deviation $\delta_{L\sigma}$. The scatter is quoted in natural log space. The fitted model is plotted along with the data in Fig. 5. The fitted normalization and slope were $A_{M\sigma} = 0.48 \pm 0.09$ and $B_{M\sigma} = 1.34 \pm 0.44$, respectively, assuming $M_0 = 1.5 \times 10^{14}$ M$_\odot$ and $\sigma_0 = 400$ km s^{-1}. The measured slope is in tension

[2]LIRA is available as an R package from https://cran.r-project.org/web/packages/lira/index.html
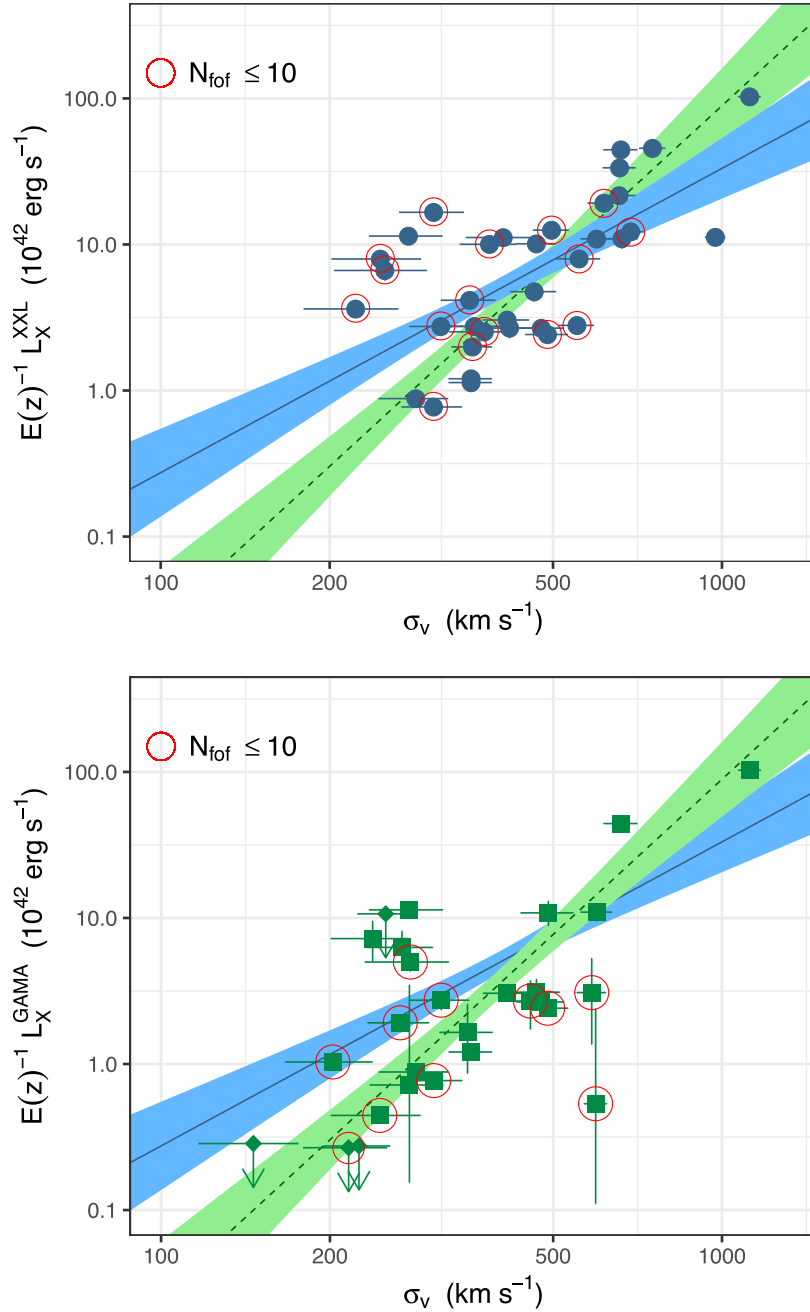
Figure 6. $L_X - \sigma_v$ relation for the XXL (upper, light blue circles) and GAMA (lower, dark green squares with upper limits given by the dark green diamonds with downward arrows) selected cluster samples. In both plots, the LIRA fit (not accounting for selection, see Section 5.2) to the X-ray selected sample is given by the blue solid line and the 1σ uncertainty is given by the light-blue shaded region. The LIRA fit to the GAMA selected sample is given by the green dashed line and the corresponding 1σ uncertainty given by the light green shaded region.

from the self-similar expectation (where $M \propto \sigma^3$) and found from simulations (e.g. Evrard et al. 2008). This is discussed further in Section 6.4.

5.2 The scaling of L_X and σ_v

The $L_X^{XXL} - \sigma_v$ (upper plot) and $L_X^{GAMA} - \sigma_v$ (lower plot) relations are presented in Fig. 6. In each case, a fit to the data using a power

law of the form

$$\left(\frac{L_X}{L_0}\right) = E(z)^{\gamma_{L\sigma}} A_{L\sigma} \left(\frac{\sigma_v}{\sigma_0}\right)^{B_{L\sigma}} \tag{4}$$

was performed. Unless stated otherwise, we used $L_0 = 5 \times 10^{42}$ erg s^{-1} and $\sigma_0 = 400$ km s^{-1}. As in Section 5.1, the model was fit to the data using LIRA.

In the case of the GAMA sample, four of the X-ray luminosity measurements are upper limits. LIRA treats these upper limits as

Table 3. Scaling parameters for the luminosity and σ_v relations modelled in this work taking the form $L/L_0 = E(z)^{\gamma_{L\sigma}} A_{L\sigma} (\sigma_v/\sigma_0)^{B_{L\sigma}}$ and $\sigma_v/\sigma_0 = A_{\sigma L}(L/E(z)^{\gamma_{L\sigma}} L_o)^{B_{\sigma L}}$, where $L_0 = 5 \times 10^{42}$ erg s^{-1}, $\sigma_0 = 400$ km s^{-1}, and $\gamma_{L\sigma} = 1$. The fit highlighted in bold represents our main result obtained via the bias correction method (see Section 5.3).

Relation (1)	Fit (2)	$A_{L\sigma}$ (3)	$B_{L\sigma}$ (4)	$\delta_{L\sigma}$ (5)
$L_X^{\mathrm{XXL}} - \sigma_v$	LIRA	0.98 ± 0.17	2.08 ± 0.48	0.89 ± 0.06
$L_X^{\mathrm{GAMA}} - \sigma_v$	LIRA	0.70 ± 0.16	3.53 ± 0.59	0.33 ± 0.14
$L_X^{\mathrm{XXL}} - \sigma_v$	**bias-corrected**	**0.37 ± 0.12**	**3.95 ± 0.57**	**1.16 ± 0.25**
		$A_{\sigma L}$	$B_{\sigma L}$	$\delta_{\sigma L}$
$\sigma_v - L_X^{\mathrm{XXL}}$	LIRA	1.08 ± 0.06	0.22 ± 0.05	0.28 ± 0.02
$\sigma_v - L_X^{\mathrm{GAMA}}$	LIRA	1.09 ± 0.07	0.26 ± 0.04	0.10 ± 0.03

(1) Relation; (2) fit method; (3) normalization; (4) slope; and (5) intrinsic scatter.

truncated probability distributions. Given an upper limit u in the GAMA-selected sample, we modelled the distribution as a normal distribution with mean equal to $u/2$ and variance equal to $u^2/12$ for values less than u, and it is null otherwise.

The results of the fits to the XXL and GAMA samples are given in Table 3. Comparing the LIRA fits for the two samples, we find that the normalization of the $L_X^{\mathrm{GAMA}} - \sigma_v$ relation is lower than the $L_X^{\mathrm{XXL}} - \sigma_v$ relation; however, the difference is only significant at the $\approx 1\sigma$ level (considering just the value of the normalization i.e. not including the scatter). When comparing the slopes, we find that the slope of the $L_X^{\mathrm{GAMA}} - \sigma_v$ is steeper than the $L_X^{\mathrm{XXL}} - \sigma_v$ relation, however, this is only significant at the $\sim 2\sigma$ level (owing to the large errors). The intrinsic scatter of the data is found to be significantly lower for the optically selected clusters ($\delta_{L\sigma} = 0.33 \pm 0.14$) than for the X-ray selected sample ($\delta_{L\sigma} = 0.89 \pm 0.06$). This result is contrary to the result found in Andreon et al. (2016), who find that the scatter of their optically selected luminosity–mass relation is 2.7 times higher than an X-ray selected relation (when including the cluster core region in the luminosity measurement, as done in this work). Upon inspection of the X-ray selected data (see Fig. 6, top plot), there are a population of outliers at luminosities $\sim 10^{43}$ erg s^{-1} that are likely driving the larger value of the scatter in the X-ray selected sample. Two of these clusters appear to host a cool-core (through visual inspection of their X-ray emission), which would explain their high L_X at a given σ_v. However, the three remaining clusters have unremarkable X-ray emission (no evidence of hosting a cool-core or other physical processes e.g. major merger). Each of these clusters have an $N_{\mathrm{fof}} < 10$, which may effect the measurement of their σ_v, but we note that many of the clusters in the bulk of the population also have $N_{fof} < 10$. Therefore, their presence as outliers is so far unexplained. Removal of these five clusters result in scaling parameters ($A_{L\sigma} = 0.64 \pm 0.11$, $B_{L\sigma} = 3.11 \pm 0.44$, and $\delta_{L\sigma} = 0.69 \pm 0.05$) in better agreement with the GAMA-selected relation. We find that the scatter of the X-ray selected sample excluding these outliers, while still a factor two times higher than the GAMA selected sample, is no longer significant. We further note that the difference in the two samples is not thought to be due to the low number of members for clusters in the two subsamples. Ruel et al. (2014) found that clusters with only a small number of velocities does not introduce bias in the measurement of the velocity dispersion in an ensemble sense. Ruel et al. (2014) also shows that the relative scatter in the velocity dispersion when using only 10 members, as compared to >35 members, is ~ 5 per cent. While the C1 selected samples contains slightly more clusters with $N_{fof} < 10$ than the GAMA selected sample, the effect will not be significant on the comparison

of the two relations. Due to the overall small number of clusters in the sample, and the dependence of the scatter on a number of outliers, robust conclusions on the scatter will need to wait until larger samples of clusters with overlapping multiwavelength contiguous areas.

While the vast majority of the literature involve studies of the $L_X - \sigma_v$ relation, it is beneficial to also investigate the form of the $\sigma_v - L_X$. Using L_X as the independent variable, the selection biases should be minimized. The fit to the data takes the form:

$$\left(\frac{\sigma_v}{\sigma_0}\right) = A_{\sigma L} \left(\frac{L_X}{E(z)^{\gamma_{\sigma L}} L_0}\right)^{B_{\sigma L}} \tag{5}$$

where $\sigma_0 = 400$ km s^{-1} and $L_0 = 5 \times 10^{42}$ erg s^{-1}. Table 3 gives the results of the fits to the XXL and GAMA samples. In contrast to the $L_X - \sigma_v$ relation, we find that the normalization and slope of the XXL and GAMA $\sigma_v - L_X$ relations are very consistent. This is likely due to the diminished effects of selection when using L_X as the independent variable. However, the trend of increased scatter in the XXL selected sample over the GAMA selected sample is still present, with the XXL sample scatter being 2.7 times larger than the GAMA sample (significant at the 4.9σ level). The $\sigma_v - L_X$ relation is shown in Fig. 10(b) and discussed further in Section 6.1.

5.3 The bias-corrected $L_X - \sigma_v$ relation

While we find a significantly lower scatter of the $L_X^{\mathrm{GAMA}} - \sigma_v$ relation compared to the $L_X^{\mathrm{XXL}} - \sigma_v$ relation, the comparison is complicated due to the well-known selection effects in X-ray selected cluster samples. Using our knowledge of the XXL selection function, we are able to correct for these effects for a more robust comparison. The XXL selection function is fully described in XXL paper II, and its implementation in a regression model is described in XXL Paper III. In the current work, we use the 'XXL likelihood' from XXL Paper III, which is translated directly to our analysis by substituting σ_v in place of the X-ray temperature.

The likelihood requires a description of the population distribution of σ_v for the clusters. This is obtained by using the $M_{WL} - \sigma_v$ relation presented in Section 5.1 to convert from a theoretical mass function (assuming the halo mass function from Tinker et al. 2008) into a σ_v function. We note however that this process ignores any correlation between σ_v and L_X for a given mass, the same drawback in the XXL paper II LT analysis. Furthermore, we include an incompleteness factor of 0.9 to account for the fact that the X-ray sample is 90 per cent complete.
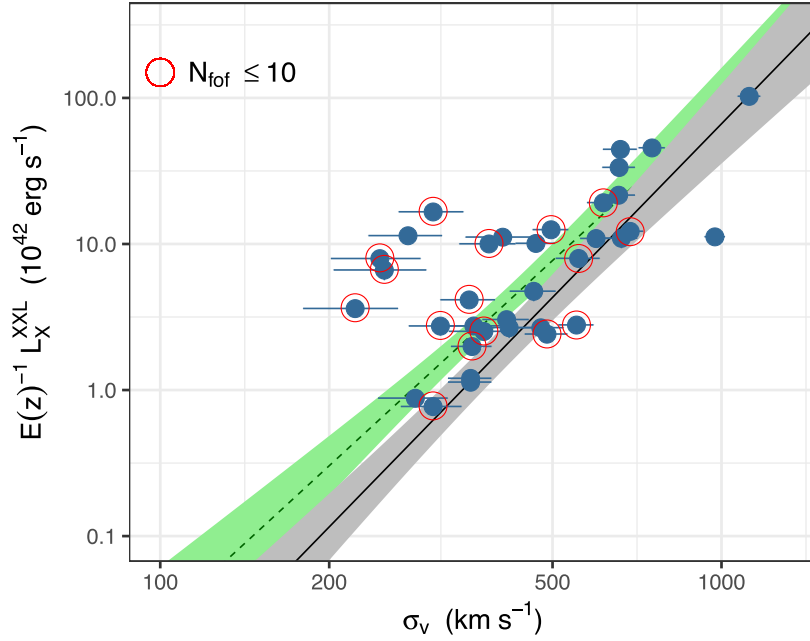
Figure 7. Bias corrected $L_X^{XXL} - \sigma_v$ relation with the best-fitting model. The light blue circles show the XXL selected clusters. The best-fitting bias-corrected model is shown as the solid black line and the 1σ uncertainty represented by the grey shaded region. The $L_X^{GAMA} - \sigma_v$ relation found using the LIRA fit (see Section 5.2) is given by the green dashed line (and the corresponding 1σ uncertainty given by the green shaded region).

The posterior distribution was analysed using the Bayesian inference package LAPLACE'S DEMON[3] version 15.03.19, within the *R* statistical computing environment (R Core Team 2014).

The bias-corrected $L_X^{XXL} - \sigma_v$ relation is plotted in Fig. 7. The fitted parameter values and their uncertainties are summarized by the mean and standard deviation of the posterior chains for each parameter. The values are given in Table 3, and their distributions are illustrated in Fig. 8. We find a normalization and slope of $A_{L\sigma} = 0.37 \pm 0.12$ and $B_{L\sigma} = 3.95 \pm 0.57$, respectively. While the difference in the normalizations of the X-ray and GAMA selected $L_X - \sigma_v$ relations is not strongly significant (see Section 5.2), it is interesting to note that the normalization of the bias-corrected relation is now lower than the $L_X^{GAMA} - \sigma_v$ relation. We find that the normalization of the bias-corrected $L_X^{XXL} - \sigma_v$ relation is 0.53 ± 0.21 times lower than the GAMA selected relation (significant at the 1.7σ level). Furthermore, the lower normalization could be driven by the steeper slope of the bias-corrected relation (when compared to the uncorrected $L_X^{XXL} - \sigma_v$ relation in Section 5.2), which now agrees well with the $L_X^{GAMA} - \sigma_v$ relation slope. We also find that our modelling of the selection effects increases the inferred intrinsic scatter in the $L_X^{XXL} - \sigma_v$ relation (which is expected since neglecting selection effects ignores the undetected low luminosity tail of the scatter). While the size of the tension between the scatter in the optically and X-ray selected samples has increased (with the intrinsic scatter in the $L_X^{GAMA} - \sigma_v$ relation 3.5 times lower than that of the bias-corrected $L_X^{XXL} - \sigma_v$ relation), the significance has also decreased, now only at the 2.9σ level. The scatter in these relations is discussed further in Section 6.2.
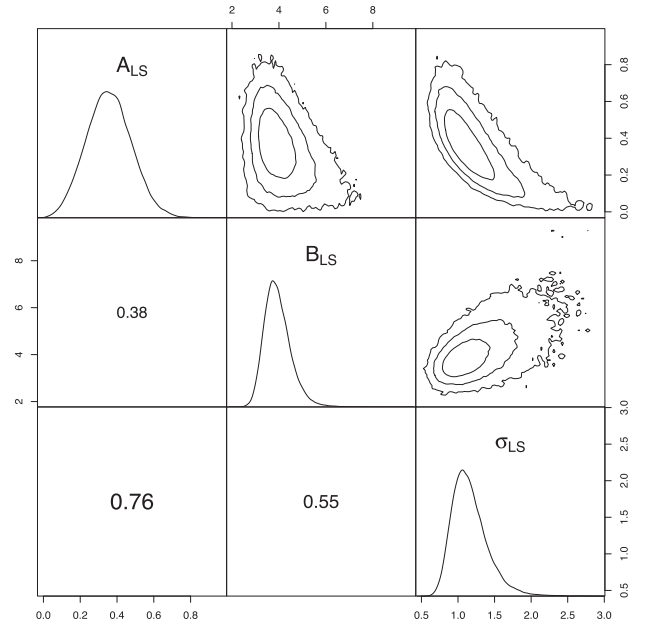

Figure 8. Scatterplot matrix for the fit of the bias corrected $L_X^{XXL} - \sigma_v$ relation of the X-ray sample. The posterior densities are shown along the diagonal; the 1, 2, and 3σ confidence contours for the pairs of parameters are shown in the upper right panels. The lower left panels show the Pearson's correlation coefficient for the corresponding pair of parameters (text size is proportional to the correlation strength).

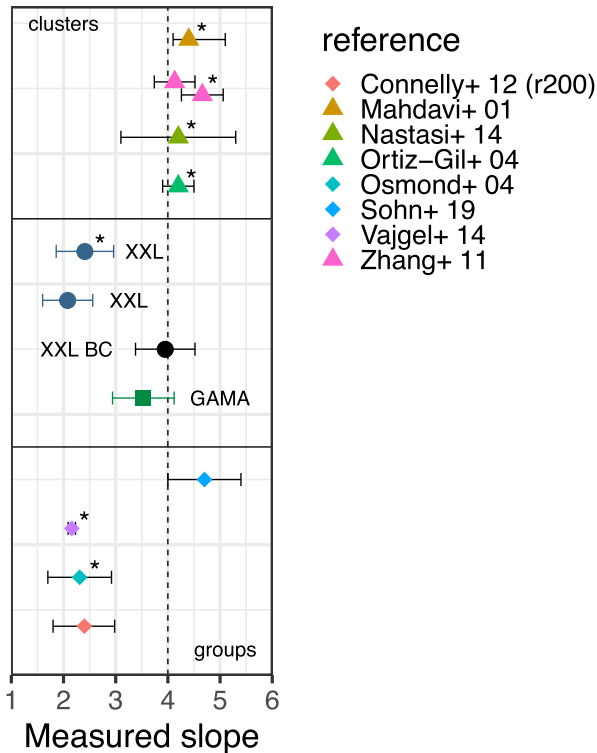[3]https://github.com/LaplacesDemonR/LaplacesDemon

Figure 9. Non-comprehensive compilation of the measured slope of the $L_X - \sigma_v$ relation as taken from Lovisari et al. (2021). The soft-band and bolometric XXL (blue circles), XXL bias corrected (XXL BC, black circle), and GAMA (green square) slopes are highlighted for comparison (values taken from Table 3). The self-similar expectation is given by the vertical dashed line. ∗ highlights relations that consider bolometric luminosities.

6 DISCUSSION

6.1 Comparison to previously published relations

The $L_X - \sigma_v$ relation, in comparison to other scaling relations, is not well studied and therefore direct comparisons to this work are challenging (e.g. others use different energy bands, different extraction radii, different instruments, and core exclusion/inclusion). Furthermore, the majority of literature studies analysed clusters with notable X-ray emission. The scatter of luminous objects can be smaller than considering the full mass range. In the literature, results vary, with some finding a slope steeper than that of the self-similar expectation (e.g. Mahdavi & Geller 2001; Hilton et al. 2005; Zhang et al. 2011), and other finding a shallower slope than self-similar (e.g. Connelly et al. 2012). The state of the literature was recently summarized in Lovisari et al. (2021). Based upon fig. 5 in Lovisari et al. (2021), we summarize our results in the context of previous group and cluster studies of the $L_X - \sigma_v$ relation. Fig. 9 shows the XXL, XXL bias-corrected, and GAMA $L_X - \sigma_v$ relations found in this work, compared to the non-comprehensive compilation of measured slopes in the literature taken from Lovisari et al. (2021). The expected self-similar evolution is given by the vertical dashed line. Note however, that the self-similar expectation changes depending on the temperature range covered and the energy band used to measure the luminosity (see Lovisari et al. 2021, for a full discussion). We discuss in depth comparisons below.

For the first comparison, we made use of the luminosity and velocity dispersion data presented in Zhang et al. (2011, hereafter Z11), based on the X-ray selected HIFLUGCS survey. We use this study as it is one of the few studies that matches as closely as possible the data analysis used in this work i.e. luminosities obtained from *XMM* and derived within r_{500}. We note however that the Z11 sample contains more massive clusters, with the majority of their cluster having $\sigma \gtrsim 400 \, \text{km s}^{-1}$. In order to avoid mis-interpretations of the comparison with Z11, we make use of the data provided in Z11 (see tables 1 and C.1 in Z11) and refit using the LIRA fitting method as used in Section 5.2. However, only bolometric luminosities are provided in Z11 and we therefore compare to bolometric luminosities derived for our XXL C1 selected sample. The bolometric luminosities are estimated via the same method as described in Section 3.1, and determined over the energy range 0.01–100 keV.

We fit to both our XXL selected sample and the Z11 sample assuming equation (4) (with $L_0 = 1 \times 10^{43}$ erg s^{-1} and $\sigma_0 = 500$ km s^{-1}). The data and relations of the Z11 data and our XXL sample are shown in Fig. 10(a). The fit to the Z11 data yields a normalization and slope of $A_{L\sigma, Z11} = 6.21 \pm 1.03$ and $B_{L\sigma, Z11} = 3.49 \pm 0.30$. When comparing to the XXL $L_X^{bol} - \sigma_v$ relation where $A_{L\sigma} = 1.55 \pm 0.28$ and $B_{L\sigma} = 2.41 \pm 0.55$, we find some clear differences. While the slope of the Z11 sample is steeper than our XXL sample, the difference is only significant at the $\sim 1.7\sigma$ level, however the normalization of the Z11 is significantly higher than the XXL sample. One plausible cause is that this offset is due to the presence of very strong cool-core clusters in the HIFLUCGS sample that is not present in the XXL sample. A similar argument was made in XXL Paper III when comparing the brightest 100 XXL cluster sample to the REXCESS clusters sample.

The second sample we compare to is the sample of X-ray selected groups detected in the COSMOS (Scoville et al. 2007) field, as studied in Gozaliasl et al. (2020, hereafter G20). This sample spans a comparable range of X-ray luminosity and velocity dispersion as our XXL selected sample, and constructed from a contiguous survey region. G20 find a slope of the $\sigma_v - L_X$ relation of $B_{\sigma L, G20} = 0.026^{0.055}_{0.056}$, note the change in regression such that σ_v is regressed against L_X. We compare the G20 relation with the $\sigma_v - L_X^{XXL}$ relation found in Section 5.2. The $\sigma_v - L_X^{XXL}$ relation is plotted in Fig. 10(b), with the LIRA fit given by the blue solid line. The relation as presented in G20 is highlighted by the dashed white line (with the orange shaded region representing the 1σ uncertainty about the mean relation). There is a striking difference in the slopes of the two samples, with the G20 relation appearing flat compared to the XXL C1 relation. However, given the large errors on the relations for both samples, the difference in the slopes is only significant at the 2.8σ level. We note that that the G20 sample contains a larger proportion of low luminosity systems compared to the sample studied in this work. We therefore create a low mass sub-set of our clusters, refit, and compare this sub-set to the G20 relation. For the low mass sub-set, we take clusters with a mass $<10^{14} \, \text{M}_\odot$ (as estimated from the the $M_{WL} - \sigma_v$ in Section 5.1). Using these clusters, we find a slope of the $\sigma_v - L_X$ of 0.05 ± 0.06. This value is consistent with the value found in G20.

The final sample compared to is one constructed from The SPectroscopic Identification of *eROSITA* Sources (SPIDERS; Clerc et al. 2020). Briefly, SPIDERS is a spectroscopic follow-up effort as a part of the Sloan Digital Sky Survey IV (SDSS-IV), used for the identification of X-ray clusters drawn from CODEX (Finoguenov et al. 2020) and X-CLASS (Clerc et al. 2016), and contains 2740 confirmed galaxy clusters. In Kirkpatrick et al. (2021, hereafter K21), using a sub-set of 755 with the most robust velocity dispersion measurements, they produced a $\sigma_v - L_X$ relation using the largest number of high mass clusters to date. This relation is plotted in Fig. 10(b), given by the thick black dashed line (and the turquoise
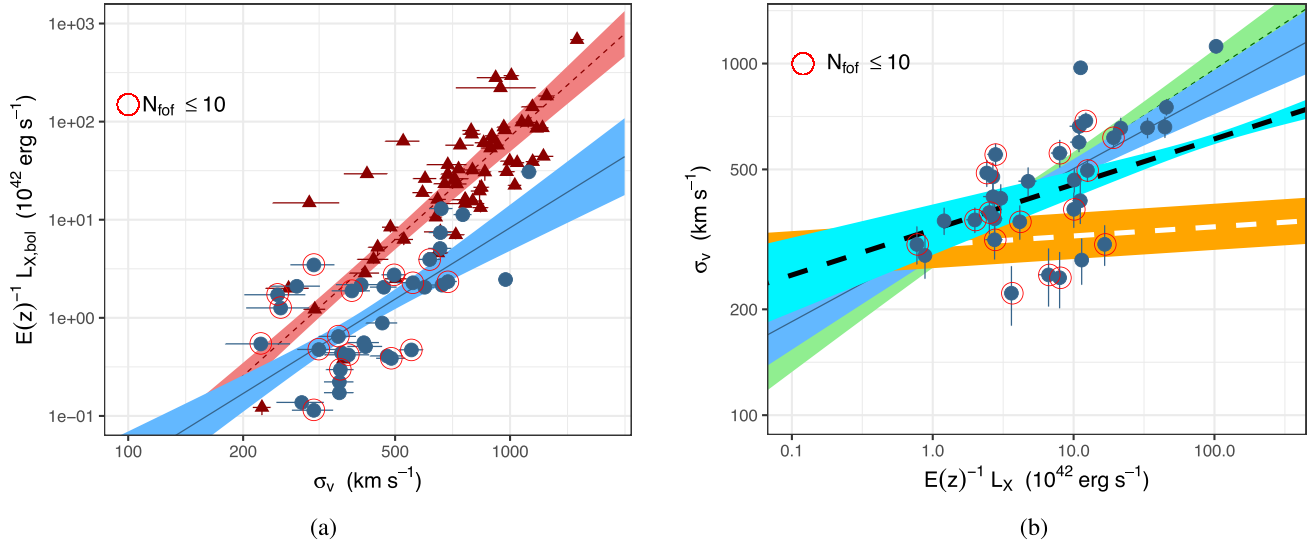
Figure 10. (a): $L_{X,bol} - \sigma_v$ relation for the XXL C1 selected sample, the LIRA fit (not accounting for selection) is given by the blue solid line. The HIFLUCGS sample is overplotted (given by the dark red triangles) and the corresponding LIRA fit is given by the red dashed line. (b): $\sigma_v - L_X^{XXL}$ relation for the XXL C1 selected sample, the LIRA fit (not accounting for selection) is given by the blue solid line. The corresponding relation for the GAMA selected sample is given by the green dashed line. The relations given in Gozaliasl et al. (2020) and Kirkpatrick et al. (2021) are highlighted by the thick white and black dashed lines, respectively. In all cases, the shaded regions represent the 1σ uncertainty.

shaded region representing the 68 per cent confidence). While the slope appears shallower than that measured for the XXL and GAMA samples, the slope of the K21 relation is consistent with that measured in this work. Note that the relation given in K21 is fit to bias corrected bi-weight velocity dispersions and luminosities determined within the 0.1–2.4 keV band. These differences are not accounted for in this comparison.

6.2 Comparison of the scatter

In this section, we address the question of whether the scatter in X-ray luminosity is significantly larger in optically selected samples than those selected in X-rays.

A study by Andreon et al. (2016) compared the scatter in luminosity in the $L_X - M$ relation (δ_{LM}) of an optically selected cluster sample with that of the X-ray selected REXCESS sample of Pratt et al. (2009). Our study can be usefully compared to that work, with the advantage that the same X-ray and optical analysis are used for both the X-ray and optically selected samples. Note that since our work studies the $L_X - \sigma_v$ relation, we make comparisons with the results of Andreon et al. (2016) that used masses derived from σ_v. This means that it is reasonable to compare the change (rather than the actual values) in δ_{LM} between X-ray and optically selected samples from Andreon et al. (2016) to the results found for $\delta_{L\sigma}$ in our work.

Andreon et al. (2016) found that δ_{LM} was 2.7 times larger for their optically selected sample than for the REXCESS X-ray selected sample. In this work, we find results contrary to that found in Andreon et al. (2016), such that the scatter of our optically selected sample is lower than the X-ray selected sample. We find $\delta_{L\sigma}$ in our optically selected sample is 2.8 times lower than that in the X-ray selected sample, increasing to 3.4 times lower when the X-ray selection biases are modelled.

Looking at the magnitude of the scatter in these different studies, we can see that the large difference in scatter between our X-ray and optically selected samples is mainly due to the fact that the

scatter in our X-ray selected sample is larger than than that in the REXCESS sample. Andreon et al. (2016) found $\delta_{LM} = 1.08 \pm 0.16$ in their optically selected sample (converting their scatter to natural log). This is significantly larger than the value of $\delta_{L\sigma} = 0.31 \pm 0.13$ we find in our GAMA-selected sample. Meanwhile, the scatter of $\delta_{LM} = 0.41 \pm 0.07$ in the REXCESS sample (Pratt et al. 2009) is notably smaller (at 3.1σ significance) than the value of $\delta_{L\sigma} = 1.16 \pm 0.25$ in our XXL-selected sample. The difference remains significant if we compare with the value of $\delta_{L\sigma} = 0.89 \pm 0.06$ we find for the XXL sample without modelling selection biases, which is more consistent with the REXCESS results, where their measured scatter is not corrected for selection biases.

The fact that we find that $\delta_{L\sigma}$ in our X-ray selected sample is significantly larger than δ_{LM} in the REXCESS sample is likely due to the fact that the masses used to infer δ_{LM} in Pratt et al. (2009) are derived from Y_X (the produce of gas mass and temperature). Y_X is known to be a good mass proxy (e.g. Kravtsov, Vikhlinin & Nagai 2006; Maughan 2007), but the high degree of covariance between L_X and gas mass will act to suppress the apparent scatter in the $L_X - M$ relation (Maughan 2014; Andreon et al. 2016).

A more direct comparison of the scatter for an X-ray selected sample is that of Z11, as done in Section 6.1 above. For the Z11 sample, we find $\delta_{L\sigma} = 0.83 \pm 0.09$ based upon the fitted in in Section 6.1. This agrees extremely well with the scatter we find in our X-ray selected sample (without correction for X-ray selection biases, which is the most comparable with Z11).

Another point of comparison is Connelly et al. (2012, hereafter C12), wherein the $L_X - \sigma_v$ relations of optically and X-ray selected samples from the same surveys were measured. The samples used were of similar size to our work, but covered a broader redshift range, with $0.1 < z < 0.8$ for the X-ray selected clusters and $0.1 < z < 0.5$ for the optically selected clusters. C12 measured $\delta_{L\sigma}$ for several sub-sets and different apertures, finding that $\delta_{L\sigma}$ for the X-ray selected systems to be marginally lower than, or consistent with, that of the optically selected sample (see C12, table 10). Once again, this is opposite to our results. The values of $\delta_{L\sigma}$ for the X-ray

selected sample measured by C12 (ranging from $\delta_{L\sigma} = 0.19^{+0.13}_{-0.09} - 0.43^{+0.08}_{-0.06}$ depending on the quality of the X-ray data used and the radius within which to derive the luminosities) tend to be significantly smaller than the values we find for our corresponding X-ray sample. Interestingly, the value of $\delta_{L\sigma}$ for their optically selected sample is entirely consistent with that measured for our GAMA selected sample. A more detailed comparison is not possible given the significant differences in methodology between C12 and our work.

Our overall conclusion from these comparisons is that our result that the scatter of X-ray selected samples is significantly larger than optically selected sample, is in tension with previous studies. However, the comparison of the scatter values (i.e. when comparing our X-ray selected sample to previous X-ray selected samples) to published results is inconclusive. Therefore, validation of our scatter values will require further work.

6.3 Exploring the nature of X-ray undetected GAMA clusters

Our optically selected cluster sample contains 13 GAMA sources that are not matched to a C1 or C2 defined XXL cluster (hence lacking in significant X-ray emission). These cases are discussed individually in Section 4.2. For six clusters, the non-detection can be explained by the low effective exposure and/or large off-axis angle of the group in the *XMM* observations. For the remaining eight clusters, the lack of a significant cluster detection appears to be due to a low X-ray luminosity of the cluster. One possible explanation for a deficit of X-ray emission would be if the gas within the cluster has not yet reached the virial temperatures required to emit at X-ray wavelengths, suggesting that the undetected GAMA systems are young and still in the process of forming. Cosmological simulations have shown that the apparent magnitude gap (Δm_{12}) between the brightest cluster galaxy (BCG) and second-brightest cluster galaxy can give an indication of the cluster age (e.g. Dariush et al. 2010; Cui et al. 2011; Raouf et al. 2014; Raouf, Khosroshahi & Dariush 2016). Low values of Δm_{12} also indicate that the system may be undergoing a merger, where the addition of bright galaxies reduces Δm_{12}. We therefore examined the distribution of Δm_{12} of the GAMA selected sample.

Fig. 11 plots the distribution of Δm_{12} for the GAMA selected sample, as a function of the offset of the cluster from the $L_X^{GAMA} - \sigma_v$ relation (Fig. 7, bottom plot). The offset was defined as the ratio of the measured luminosity, to the luminosity calculated based upon the clusters' σ_v and the $L_X^{GAMA} - \sigma_v$ relation (this ratio is defined as L_X^{GAMA}/L_{σ_v}). The clusters are split between those with a significant X-ray detection (red diamonds) and GAMA clusters with no significant X-ray detection (blue squares). Undetected GAMA clusters with an upper limit luminosity measurement are denoted with a left facing arrow.

As shown in Fig. 11, visually, there appears to be two trends in the data. First, all of the detected GAMA clusters have a $\Delta m_{12} > 0.3$ (denoted by the dashed black line in Fig. 11) and there is a larger scatter of Δm_{12} values for GAMA undetected clusters. Secondly, the majority of GAMA clusters sitting above the $L_X^{GAMA} - \sigma$ relation (i.e. $L_X^{GAMA}/L_{\sigma_v} > 1$) again have $\Delta m_{12} > 0.3$, irrespective of their X-ray detection. The low values of Δm_{12} for many of the undetected GAMA clusters leads to two interpretations of the lack of X-ray emission; (i) the clusters are still in the process of forming and the gas has yet to reach virial temperatures, (ii) the clusters are in the process of merging, and hence have a low X-ray surface brightness (Burns et al. 2008). Interestingly, Gozaliasl et al. (2019) find a correlation of the magnitude gap and the offset between the brightest group galaxy
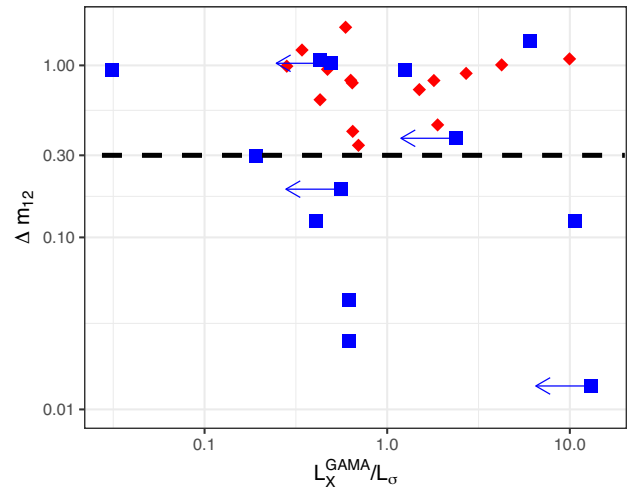

Figure 11. Plot of the GAMA selected clusters showing the apparent magnitude gap (Δm_{12}) between the first and second brightest cluster galaxy as a function of the ratio of the measured L_X^{GAMA} to the L_{σ_v}. Red diamonds represent an X-ray detected GAMA cluster and blue squared represent the 13 undetected GAMA clusters. Undetected GAMA clusters with upper limit luminosities are represented by a left facing arrow. The black dashed horizontal line at $\Delta m_{12} = 0.3$ represent the region devoid of X-ray detected GAMA clusters (see Section 6.3).

(BGG) and the X-ray peak (BGG$_{offset}$). They found the BGG$_{offset}$ negatively correlates with Δm_{12}, indicating low Δm_{12} groups may indeed be in the process of merging, with Lopes et al. (2018) showing large offset systems appear disturbed. Due to the non-detection of many of the GAMA selected groups, further investigation using these diagnostics is limited until deeper observations are available.

While a per cluster investigation is not possible, to investigate them further, we performed a detailed stacking analysis of all 13 GAMA sources without extended emission to find hints of any excess emission. The stacking analysis is described fully in Willis et al. (2018) and we briefly review the process here. We extract cut-outs from the EPIC images in the (0.5–2) keV band. These cut-outs are centred on the galaxy at the iterative centre of the cluster, and have a size of 2×2 Mpc at the redshift of the cluster redshift. Corresponding cut-outs of the exposure map are also obtained. Background cut-outs are also created for each object and EPIC camera. Each exposure map is weighted by a factor of $[d_L(z)/d_L(\tilde{z})]^2$, where $d_L(z)$ is the luminosity distance to the source and $d_L(\tilde{z})$ is the luminosity distance to the mean redshift of the sample, in this case $\tilde{z} = 0.153$. Moreover, each cut-out is rescaled to a common size, i.e. 2 Mpc size at $\tilde{z}$. All detected point sources are masked out in each image, exposure and background cut-outs. We add together each of the EPIC cut-outs to produce a stacked image. We also add together each of the individual exposure and background cut-outs. In this step, the MOS exposure maps are corrected according to the MOS/PN response ratio. The final product is a count-rate image that is obtained by subtracting the stacked background map from the stacked photon image and dividing by the stacked exposure map. Fig. 12(a) shows the stacked image of the 13 undetected GAMA clusters. We produce a radial profile of the stacked count-rate image, Fig. 12(b, black points), where the errors are the 68 per cent errors obtained through a bootstrap analysis. The solid black region comprises the background, obtained by using 500 stacks of random positions in the XXL survey, using the same number of unmatched GAMA clusters.
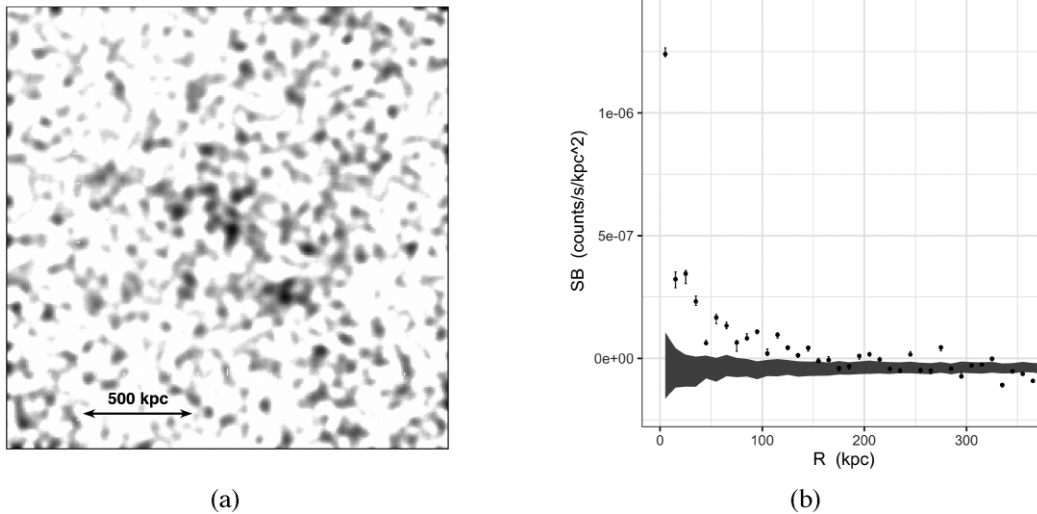
Figure 12. (a) Stacked X-ray photon image of 13 GAMA sources without significant extended emission. (b) Radial profile of the stacked GAMA images, given by the black points. The solid black region comprises the background, obtained by using 500 stacks of random positions in the XXL survey, using the same number of unmatched GAMA clusters.

The radial profile appears to have significant emission (above the background level) in the core region, assuming a core radius of a standard β-profile of $r_c = 150$ kpc as done in XXL. The lack of extended emission outside of the core from the stacked image favours the interpretation that the gas in these systems has yet to reach virial X-ray temperatures. With each image in the stack centred on the GAMA BCG, the X-ray emission could be associated with galactic emission. However, one cannot exclude the possibility that these groups are high entropy systems whereby the hot group gas has low density, and hence low surface brightness (Pearson et al. 2017).

6.4 Dependence of the $L_X - \sigma_v$ on the assumed $M_{WL} - \sigma_v$ relation

As found in Section 5.1, the measured slope of the $M_{WL} - \sigma$ relation is in tension with the self-similar expectation. Furthermore, simulations estimate a slope consistent with the self-similar expectation (e.g. Evrard et al. 2008; Caldwell et al. 2016; Armitage et al. 2018). Therefore, to investigate the impact on the assumed shape of the $M_{WL} - \sigma_v$ relation on the $L_X - \sigma_v$ relation, we repeat our analysis with the slope of the $M_{WL} - \sigma_v$ relation fixed at $B_{M\sigma} = 3$ (i.e. repeating the fitting detailed in Section 5.1 and fitting just for the normalization).

Table A1 presents the results of the fits to the XXL and GAMA samples using LIRA, and XXL bias-corrected fits. Comparing the LIRA fits to our results in Table A1, using our standard analysis (by fitting for both the slope and normalization in the $M_{WL} - \sigma_v$ relation), we find the results are consistent. This is somewhat unsurprising as the $M_{WL} - \sigma$ relation in the LIRA analysis is used purely for extrapolation of luminosities out to r_{500} (from the spectral extraction region of 300 kpc), with luminosity being centrally concentrated. Furthermore, the comparison of the XXL and GAMA relations show the same trend when comparing the scatter of the two relations (i.e. a significantly higher scatter for the XXL sample than the GAMA sample), as found in Section 5.2. However, when performing the bias-correct fit, the difference to the standard analysis becomes more pronounced. During the bias-correction, the $M_{WL} - \sigma_v$ relation is again used for extrapolation out to r_{500}, but

also for the conversion of the mass function to a σ_v function. We find that the normalization of the $L_X - \sigma_v$ relation is ≈ 9 times lower than the standard bias-corrected fit, somewhat attributed to the steeper slope (a factor ≈ 1.6 times steeper). Although we find these differences, owing to the large errors, the bias-corrected relation is not significantly different to the bias-corrected relation when fitting for the slope of the $M_{WL} - \sigma_v$ relation. As found above when comparing between the XXL and GAMA LIRA fits, the bias-corrected scatter for the X-ray sample is still significantly higher than the GAMA selected sample. Therefore, the assumption of the slope for the $M_{WL} - \sigma_v$ relation does not change this observed trend.

7 CONCLUSIONS

The $L_X - \sigma_v$ relation has been studied using two samples of clusters, one sample constructed based upon their X-ray emission (L_X^{XXL}), and one constructed based on their galaxy content (L_X^{GAMA}). Our main conclusions are as follows:

(i) Using a fit method that does not fully take into account the selection function, we find that the scatter of the $L_X^{XXL} - \sigma_v$ relation is 2.7 times larger than the $L_X^{GAMA} - \sigma_v$ relation. This result is in tension with previous studies that found that the scatter in optically selected clusters is larger than X-ray selected clusters.

(ii) We find that when accounting for the selection effects of X-ray selected samples, the scatter of the $L_X^{XXL} - \sigma_v$ relation becomes 3.5 larger than the $L_X^{GAMA} - \sigma$ relation (albeit with a lower significance when not accounting for selection).

(iii) Comparing to previous determinations of the scatter in the $L_X - \sigma_v$ relation, we find instances where our X-ray and optically selected relations both agree and disagree with previous results. While there are drawbacks in the comparisons, this highlights that further work is required to understand the differences in scatter between X-ray and optically selected clusters.

(iv) Examining the apparent r-band magnitude gap between the first and second brightest cluster galaxy (Δm_{12}), we find a population of GAMA systems undetected in X-rays have low values of Δm_{12}.

Furthermore, none of the GAMA detected systems appear at these low Δm_{12} values (<0.3).

(v) Stacking X-ray images of all the undetected GAMA selected clusters, reveals no significant extended X-ray emission outside the core regions. Combined with the low values of Δm_{12}, this suggests that these groups are young systems still in the process of forming.

We have found that when taking into account X-ray selection effects, the scatter of the our X-ray selected sample is larger than that of our optically selected cluster sample. However, for our optically selected sample, we find a population of undetected clusters in X-rays that appear dynamically young. In order to probe the difference in the scatter further, and the nature of the undetected systems, it is clear that future overlapping areas, such as those created by *eROSITA* (X-ray) and the Vera C. Rubin Observatory (optical), will be of paramount importance.

DATA AVAILABILITY

The data underlying this study are available in the article.

REFERENCES

Adami C. et al., 2018, A&A, 620, A5 (XXL Survey XX)
Anders E., Grevesse N., 1989, Geochim. Cosmochim. Acta, 53, 197
Andreon S., Bergé J., 2012, A&A, 547, A117
Andreon S., Serra A. L., Moretti A., Trinchieri G., 2016, A&A, 585, A147

Armitage T. J., Barnes D. J., Kay S. T., Bahé Y. M., Dalla Vecchia C., Crain R. A., Theuns T., 2018, MNRAS, 474, 3746
Baldry I. K. et al., 2018, MNRAS, 474, 3875
Beers T. C., Flynn K., Gebhardt K., 1990, AJ, 100, 32
Brough S., Forbes D. A., Kilborn V. A., Couch W., 2006, MNRAS, 370, 1223
Burns J. O., Hallman E. J., Gantner B., Motl P. M., Norman M. L., 2008, ApJ, 675, 1125
Caldwell C. E., McCarthy I. G., Baldry I. K., Collins C. A., Schaye J., Bird S., 2016, MNRAS, 462, 4117
Clerc N. et al., 2016, MNRAS, 463, 4490
Clerc N. et al., 2020, MNRAS, 497, 3976
Connelly J. L. et al., 2012, ApJ, 756, 139
Cui W., Springel V., Yang X., De Lucia G., Borgani S., 2011, MNRAS, 416, 2997
Dariush A. A., Raychaudhury S., Ponman T. J., Khosroshahi H. G., Benson A. J., Bower R. G., Pearce F., 2010, MNRAS, 405, 1873
Driver S. P. et al., 2011, MNRAS, 413, 971
Eckert D. et al., 2014, A&A, 570, A119
Eckert D. et al., 2016, A&A, 592, A12 (XXL Survey XIII)
Evrard A. E. et al., 2008, ApJ, 672, 122
Farahi A., Evrard A. E., McCarthy I., Barnes D. J., Kay S. T., 2018, MNRAS, 478, 2618
Finoguenov A. et al., 2020, A&A, 638, A114
Giles P. A. et al., 2016, A&A, 592, A3 (XXL Survey III)
Giles P. A. et al., 2017, MNRAS, 465, 858
Gozaliasl G. et al., 2019, MNRAS, 483, 3545
Gozaliasl G. et al., 2020, A&A, 635, A36
Hilton M. et al., 2005, MNRAS, 363, 661
Hinshaw G. et al., 2013, ApJS, 208, 19
Kaiser N., 1986, MNRAS, 222, 323
Kalberla P. M. W., Burton W. B., Hartmann D., Arnal E. M., Bajaja E., Morras R., Pöppel W. G. L., 2005, A&A, 440, 775
Kettula K. et al., 2015, MNRAS, 451, 1460
Kirkpatrick C. C. et al., 2021, MNRAS, 503, 5763
Kravtsov A. V., Vikhlinin A., Nagai D., 2006, ApJ, 650, 128
LaRoque S. J., Bonamente M., Carlstrom J. E., Joy M. K., Nagai D., Reese E. D., Dawson K. S., 2006, AJ, 652, 917
Le Brun A. M. C., McCarthy I. G., Schaye J., Ponman T. J., 2017, MNRAS, 466, 4442
Leccardi A., Molendi S., 2008, A&A, 486, 359
Lopes P. A. A., Trevisan M., Laganá T. F., Durret F., Ribeiro A. L. B., Rembold S. B., 2018, MNRAS, 478, 5473
Lovisari L., Reiprich T. H., Schellenberger G., 2015, A&A, 573, A118
Lovisari L., Ettori S., Gaspari M., Giles P. A., 2021, Universe, 7, 139
Mahdavi A., Geller M. J., 2001, ApJ, 554, L129
Mantz A., Allen S. W., Ebeling H., Rapetti D., Drlica-Wagner A., 2010, MNRAS, 406, 1773
Maughan B. J., 2007, ApJ, 668, 772
Maughan B. J., 2014, MNRAS, 437, 1171
Nastasi A. et al., 2014, A&A, 564, A17
Osmond J. P. F., Ponman T. J., 2004, MNRAS, 350, 1511
Pacaud F. et al., 2006, MNRAS, 372, 578
Pacaud F. et al., 2007, MNRAS, 382, 1289
Pacaud F. et al., 2016, A&A, 592, A2 (XXL Survey II)
Pearson R. J. et al., 2017, MNRAS, 469, 3489
Pierre M. et al., 2016, A&A, 592, A1 (XXL Survey I)
Pratt G. W., Croston J. H., Arnaud M., Böhringer H., 2009, A&A, 498, 361
R Core Team, 2014, R: A Language and Environment for Statistical Computing. R Foundation for Statistical Computing, Vienna, Austria http://www.R-project.org
Raouf M., Khosroshahi H. G., Ponman T. J., Dariush A. A., Molaeinezhad A., Tavasoli S., 2014, MNRAS, 442, 1578
Raouf M., Khosroshahi H. G., Dariush A., 2016, ApJ, 824, 140

Robotham A. S. G. et al., 2011, MNRAS, 416, 2640

Ruel J. et al., 2014, ApJ, 792, 45

Scoville N. et al., 2007, ApJS, 172, 1

Sereno M., 2016, LIRA: LInear Regression in Astronomy, Astrophysics Source Code Library. preprint(ascl:1602.006)

Sereno M., Ettori S., 2015, MNRAS, 450, 3675

Sereno M., Ettori S., Eckert D., Giles P., Maughan B. J., Pacaud F., Pierre M., Valageas P., 2019, A&A, 632, A54 (XXL Survey XXXVIII)

Smith R. K., Brickhouse N. S., Liedahl D. A., Raymond J. C., 2001, ApJ, 556, L91

Stanek R., Evrard A. E., Böhringer H., Schuecker P., Nord B., 2006, ApJ, 648, 956

Sun M., Voit G. M., Donahue M., Jones C., Forman W., Vikhlinin A., 2009, ApJ, 693, 1142

Tinker J., Kravtsov A. V., Klypin A., Abazajian K., Warren M., Yepes G., Gottlöber S., Holz D. E., 2008, ApJ, 688, 709

Umetsu K. et al., 2020, ApJ, 890, 148

von der Linden A. et al., 2014, MNRAS, 439, 2

Wetzell V. et al., 2021, preprint (arXiv:2107.07631)

Willis J. P., Ramos-Ceja M. E., Muzzin A., Pacaud F., Yee H. K. C., Wilson G., 2018, MNRAS, 477, 5517

Zhang Y.-Y., Andernach H., Caretta C. A., Reiprich T. H., Böhringer H., Puchwein E., Sijacki D., Girardi M., 2011, A&A, 526, A105

Zou S., Maughan B. J., Giles P. A., Vikhlinin A., Pacaud F., Burenin R., Hornstrup A., 2016, MNRAS, 463, 820

APPENDIX A: RESULTS OF $L_X - \sigma_v$ RELATION ASSUMING A FIXED SLOPE OF $M_{WL} - \sigma_v$ RELATION

Here, we give results of the $L_X - \sigma_v$ relation when assuming a self-similar slope ($B_{M\sigma} = 3$) of the $M_{WL} - \sigma_v$ relation. The results of the fits for the $L_X - \sigma_v$ relations for the XXL (LIRA), GAMA (LIRA), and XXL (bias-corrected, BC) are given in Table A1. Fig. A1 plots the $L_X - \sigma_v$ relation for the XXL sample with the bias-corrected relation given by the black line (and 1σ uncertainties highlighted by the grey shaded region), assuming a self-similar $M_{WL} - \sigma_v$ relation. The LIRA fit to the GAMA sample (assuming a self-similar $M_{WL} - \sigma_v$ relation) is given by the green dashed line and the corresponding 1σ uncertainty given by the green shaded region.
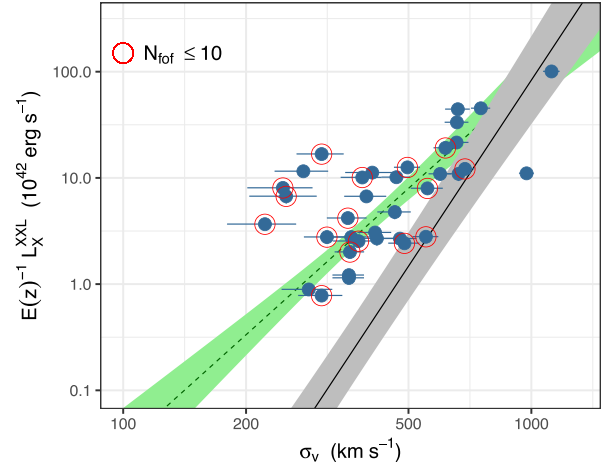

Figure A1. Bias corrected $L_X^{XXL} - \sigma_v$ relation with the best-fitting model (see Section 5.3), assuming a self-similar slope of the $M_{WL} - \sigma_v$ relation ($B_{M\sigma} = 3$). The light blue circles show the XXL selected clusters. The best-fitting bias-corrected model is shown as the solid black line the 1σ uncertainty represented by the grey shaded region. The $L_X^{GAMA} - \sigma_v$ relation found using the LIRA fit (see Section 5.2) is given by the dashed line.

Table A1. Scaling parameters for the $L_X - \sigma_v$ relations modelled in this work, assuming a self-similar slope ($B_{M\sigma}$) of the $M_{WL} - \sigma_v$ relation. The relation takes the form of $L/L_0 = E(z)^{\gamma_{L\sigma}} A_{L\sigma}(\sigma_v/\sigma_0)^{B_{L\sigma}}$, where $L_0 = 5 \times 10^{42}$ erg s^{-1}, $\sigma_0 = 400$ km s^{-1}, and $\gamma_{L\sigma} = 1$.

Relation (1)	Fit (2)	$A_{L\sigma}$ (3)	$B_{L\sigma}$ (4)	$\delta_{L\sigma}$ (5)
$L_X^{XXL} - \sigma_v$	LIRA	0.95 ± 0.17	2.37 ± 0.49	0.89 ± 0.06
$L_X^{GAMA} - \sigma_v$	LIRA	0.71 ± 0.16	3.83 ± 0.56	0.28 ± 0.12
$L_X^{XXL} - \sigma_v$	BC	0.04 ± 0.06	6.24 ± 0.67	2.16 ± 0.67

(1) Relation; (2) fit method; (3) normalization; (4) slope; and (5) intrinsic scatter.

This paper has been typeset from a TEX/LATEX file prepared by the author.